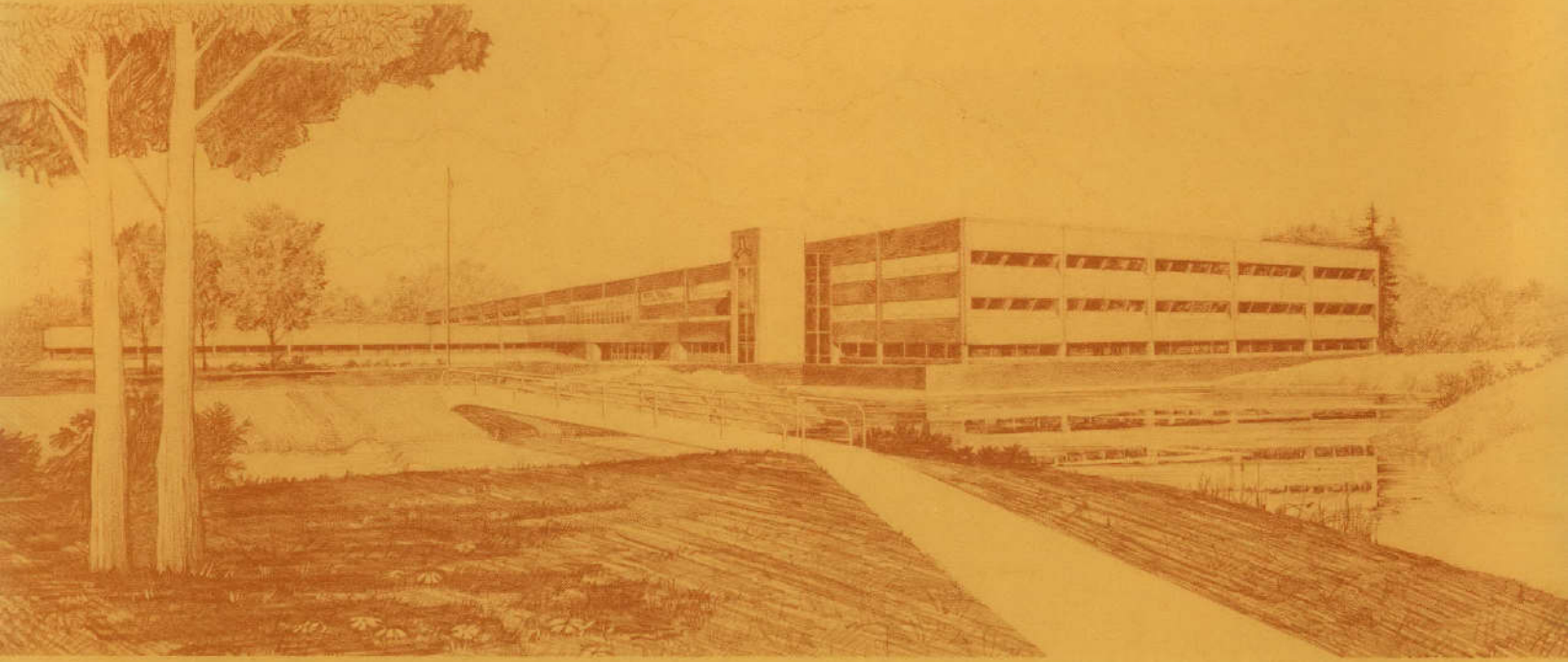# U.S. Department of Energy
Idaho Operations Office • Idaho National Engineering Laboratory

Reactivity Initiated Accident Test Series
Test RIA 1-2 Fuel Behavior Report

Beverly A. Cook
Steven K. Fukuda
Zoel R. Martinson
Patricia Bott-Hembree

January 1981

EG&G Idaho

REACTIVITY INITIATED ACCIDENT TEST SERIES TEST RIA 1-2 FUEL BEHAVIOR REPORT

Beverly A. Cook
Steven K. Fukuda
Zoel R. Martinson
Patricia Bott-Hembree

Published January 1981

EG&G Idaho, Inc.
Idaho Falls, Idaho 83415

ABSTRACT

This report presents and discusses the results from the Reactivity Initiated Accident (RIA) Test RIA 1-2 conducted in the Power Burst Facility at the Idaho National Engineering Laboratory. Four, individually shrouded, previously irradiated fuel rods were subjected to a power burst while at boiling water reactor hot-startup system conditions, resulting in an estimated axial peak, radial average fuel enthalpy of 185 cal/g (total radial average energy deposition of 240 cal/g UO_2). The test objectives were to (a) determine the enthalpy required to fail previously irradiated light water reactor fuel rods, (b) characterize the mechanism of failure, and (c) evaluate the effect of beginning-of-life and end-of-life rod internal pressures on preirradiated fuel rod response during an RIA event. The test design and conduct are described, and the test rod thermal and mechanical responses are evaluated. The failure threshold of preirradiated fuel rods and the effect of rod internal pressure on rod deformation are analyzed.

SUMMARY

The Reactivity Initiated Accident (RIA) Test RIA 1-2 was conducted in the Power Burst Facility at the Idaho National Engineering Laboratory by EG&G Idaho, Inc., for the U.S. Nuclear Regulatory Commission. The objectives of the test were to (a) determine the enthalpy required to fail previously irradiated light-water-reactor-type fuel rods, (b) evaluate the failure mechanism, and (c) study the effect of beginning-of-life and end-of-life rod internal pressures on preirradiated fuel rod response during an RIA event.

Four, individually shrouded, zircaloy-clad, UO_2 fuel rods were tested. The rods were pre-irradiated to a burnup of approximately 4800 MWd/t. Two rods were operated with an internal pressure equal to boiling water reactor (BWR) beginning-of-life conditions and two rods were pressurized to reflect BWR end-of-life internal pressures. The individual cylindrical flow shrouds were sized to provide a coolant flow volume approximately equivalent to the volume per rod in a commercial BWR bundle. The pressurized water reactor (PWR) size test rods were not typical of BWR rods, but fuel rod behavior during an RIA was expected to be roughly equivalent for PWR and BWR rod types. Starting at BWR hot-startup conditions, the rods were subjected to a power transient resulting in an axial peak, radial average fuel enthalpy of 185 cal/g (total radial average energy deposition of 240 cal/g UO_2).

The rods reached cladding peak temperatures ranging from 1520 to 1700 K during the transient, with the high pressure rods reaching lower cladding peak temperatures than the low pressure rods. Low pressure Rod 802-3 failed by means of 22 longitudinal cracks in the cladding. The other low pressure rod did not fail. The high pressure rods deformed significantly, with as much as 6.7% diametral strain with no rod failure. There was no obvious difference between the two low pressure rods that would explain the failure of one rod and not the other. However, the low pressure rod that did not fail was opened prior to the transient so that a plenum pressure sensor could be installed.

CONTENTS

FIGURES

TABLES

REACTIVITY INITIATED ACCIDENT TEST SERIES TEST RIA 1-2 FUEL BEHAVIOR REPORT

INTRODUCTION

Rapid insertion of reactivity into a light water reactor (LWR) core has long been recognized as a potential mechanism for failure of the fuel rod cladding. Extensive cladding failure and dispersal of fuel could disrupt the core such that the post-accident capability for cooling the core would be significantly impaired. To minimize the possibility of damage from postulated inadvertent reactivity initiated accidents (RIAs) in commercial LWRs, United States Nuclear Regulatory Commission (NRC) design requirements have been imposed on reactivity control systems to limit "the potential amount and rate of reactivity increase to ensure that the effects of postulated reactivity accidents can neither (a) result in damage to the reactor coolant pressure boundary greater than limited local yielding nor (b) sufficiently disturb the core, its support structure, or other reactor pressure vessel internals to impair significantly the capability to cool the core."[1] The NRC also requires that the number of fuel rods that will experience cladding failure during various RIAs be estimated and a conservative source term, subsequent transport of activity, and the resulting dose to the public be calculated.

Background to RIA Testing

Worst-case RIAs in commercial LWRs are postulated to result from the rapid removal of control rod elements from the reactor core. In a pressurized water reactor (PWR), the RIA is a result of the hypothesized mechanical rupture of a control rod drive mechanism housing or control rod drive nozzle, which results in the coolant system pressure ejecting an inserted control rod from the core. In a boiling water reactor (BWR), the worst-case RIA (rod dropout) results from (a) the separation (complete rupture, breakage, or disconnection) of an inserted control rod drive from its cruciform control blade at or near the coupling, (b) the sticking of the control blade in the inserted position as the rod drive is withdrawn, and (c) the rapid falling of the control blade to the withdrawn rod drive position.

A reactor operator (or vendor) is expected to show that

1. Reactivity excursions will not result in a radial average fuel enthalpy greater than 280 cal/g at any axial location in any fuel rod

2. Maximum reactor pressure during any portion of the assumed transient will be less than the value that will cause stresses in the reactor vessel to exceed the Emergency Condition stress limits as defined in Section III of the ASME Code

3. Offsite dose consequences will be well within the guidelines of 10 CFR 100, and are calculated assuming that any PWR fuel rod that departs from nucleate boiling fails, and any BWR rod subjected to a radial average peak fuel enthalpy of 170 cal/g or above fails.[1]

The axial peak, radial average fuel enthalpy limitation (<280 cal/g) is based on a Nuclear Regulatory Commission staff review of fuel behavior experimental data available prior to 1974. Their findings indicated that failure consequences were insignificant for total energy depositions below 300 cal/g for both irradiated and unirradiated UO_2 fuel rods subjected to rapid power excursions. Therefore, an axial peak, radial average fuel enthalpy of 280 cal/g was considered a conservative maximum limit to ensure minimal core damage and maintenance of both short- and long-term core cooling capability.[a] The guidelines regarding reactor coolant pressure boundary stresses are assumed to be met if compliance with the enthalpy limitation is satisfactorily demonstrated.

---

a. Axial peak, radial average fuel enthalpy is somewhat less than the associated total energy deposition because of heat transfer from the fuel to the cladding and coolant during the power transients and the relatively large fraction of the total energy that is due to delayed fissions (10 to 20%, depending on the reactor design).

Complex analysis techniques are used to estimate the effects of postulated RIAs in light water reactors.[2,3,4] These techniques generally couple the transient neutronics behavior, fuel rod thermal and mechanical response, and the coolant hydrodynamic response. Verification of these analytical models is incomplete, however, due to limitations of existing fuel behavior data. Much of the applicable RIA experimental data were obtained several years ago in the Special Power Excursion Reactor Test (SPERT) [Capsule Driver Core (CDC)] and Transient Reactor Test Facility (TREAT) test programs, which investigated the behavior of single or small clusters of fuel rods under atmospheric pressure and ambient temperature conditions, no forced coolant flow, and zero initial powers. Similar tests have been performed in the Japanese Nuclear Safety Research Reactor (NSRR).

In each of these facilities, a driver core with encapsulated test fuel in a central flux trap was operated to produce a power excursion. The magnitude and time duration of these excursions were comparable to those of severe, hypothesized RIAs in LWRs. The experiments were performed with single fuel rods (or a small cluster of rods) placed at the center of test capsules containing stagnant water. The initial coolant conditions for the CDC, TREAT, and NSRR tests were closely representative of BWR cold critical conditions, namely, reactor critical at a power level of 10^{-8} of rated power, coolant at 300 K, and atmospheric pressure with no flow. Energy deposition, and consequent enthalpy increase in the test fuel, was found to be the single most important independent variable. The failure threshold of unirradiated fuel rods was in the range of 205 to 225 cal/g axial peak, radial average fuel enthalpy. These enthalpies correspond to a peak fuel enthalpy near the fuel surface in the range of 260 to 265 cal/g.[a] The narrow range of values (260 to 265 cal/g) is evidence that peak fuel enthalpy near the pellet surface is the variable most important to incipient cladding failure.

Tests were performed using fuel rods previously irradiated to burnups of up to 32 000 MWd/t. Rod failures occurred at lower energy depositions in some cases than in similar tests with unirradiated fuel rods, with little sensitivity attributable to the degree of burnup. The lower

---

a. Axial peak, radial average fuel enthalpy is reported because it relates to the NRC licensing criteria.

failure threshold was not statistically established because only a few previously irradiated rods were tested. The results are plotted in Figure 1.

INEL-A-16 893
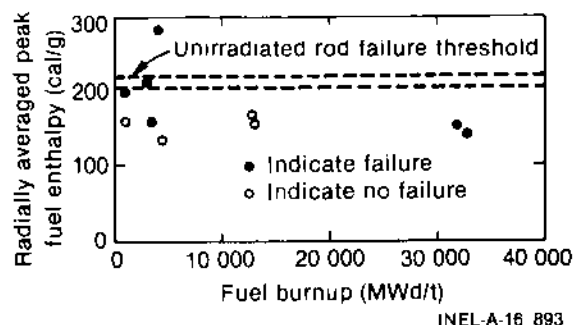
Figure 1. Failure energy as a function of burnup for irradiated rods tested in the SPERT Program.

In the CDC, TREAT, and NSRR experiments, test rods failed by cladding melting, cracking of embrittled cladding, or both. The unirradiated test rod failure threshold was found to be relatively insensitive to cladding material, cladding heat treatment, fuel form, material, and gap width. Single NSRR fuel rods within shroud enclosures failed at lower energy depositions than rods not enclosed in shrouds. The incipient failure threshold for rods enclosed in a 14-mm cylindrical shroud was found to be in the range of 210 to 245 cal/g UO_2 total energy deposition, compared with 245 to 265 cal/g UO_2 for unenclosed fuel rods. Reference 5 presents a review and summary of the SPERT and NSRR results.

Description of Test RIA 1-2

The RIA test program currently underway in the Power Burst Facility (PBF) at the Idaho National Engineering Laboratory is expected to provide RIA fuel behavior data under conditions more nearly typical of power reactor operation, thus allowing further evaluation of the NRC licensing criteria and assessment and development of analytical models. These tests are being conducted by EG&G Idaho, Inc., as part of the Nuclear Regulatory Commission's Reactor Safety Research Program.[6,7] The objectives of these RIA tests are to (a) determine fuel rod failure threshold enthalpies and failure mechanisms for both fresh and previously irradiated rods;

2

(b) determine the mechanisms and consequences of rod failure for previously irradiated and fresh fuel at (or slightly above) the NRC design limit axial peak, radial average fuel enthalpy of 280 cal/g; and (c) measure the thermal, mechanical, and chemical interaction behavior of a typical LWR fuel rod during an RIA. For each of the PBF RIA tests, the pressure, temperature, and flow rate of the coolant will be typical of hot-startup conditions in a commercial boiling water reactor.

Extensive thermal-hydraulic analyses were performed to compare the behavior of the shorter length (0.9 m) PBF test rods with full-length (3.8 m) BWR/6 fuel rods during an RIA event at BWR hot-startup conditions. The analyses indicated that for the same energy deposition and initial coolant mass flux, the PBF test rods experience nearly the same maximum cladding temperatures as the full-length power reactor fuel rods, but lower coolant outlet velocities, which cause a slower reduction in cladding temperature. The analyses indicated that the maximum cladding temperature and duration of film boiling calculated for the PBF RIA fuel rods would be most similar to the calculated RIA behavior of the commercial 3.8-m BWR/6 fuel rods if (a) the PBF rod flow shroud inner diameter was minimized, (b) the flow loss coefficient at the inlet of the PBF rod flow shroud was equivalent to the loss coefficient of a BWR/6 fuel assembly, and (c) initial PBF loop coolant conditions were equivalent to commercial BWR/6 hot-startup conditions. Nominal BWR/6 coolant conditions were incorporated into the design of the RIA tests.

The PBF was designed primarily for performing very high-power excursions. In the PBF, a power excursion is initiated by a fast-acting drive system that moves the transient rods at a velocity of 9.5 m/s, which corresponds to a reactivity addition rate of about 50$/s or a reactivity insertion time of about 50 ms. In contrast, BWRs have devices attached to the control rods to limit the rod drop velocity. The maximum control rod freefall velocity is about 1.5 m/s, which corresponds to a reactivity insertion time of about 1.15 s. Thus, in terms of rod drop speed, the PBF is not typical of a commercial power reactor. The influence of this difference in reactivity insertion times between the PBF and a BWR is somewhat mitigated since the time constant for heat transfer between the fuel and the coolant is long, compared to the reactivity insertion time for a BWR.

The PBF RIA Series I tests are listed in Table 1. Test RIA 1-2, completed November 22, 1978, was the second of six planned tests in the RIA Test Series I. The main objectives of Test RIA 1-2 were to

1. Determine the enthalpy required to fail previously irradiated LWR fuel rods

2. Characterize the mechanism of failure

3. Evaluate the effect of rod internal pressure on preirradiated fuel rod response during an RIA event.

Test RIA 1-2 consisted of a nonnuclear loop heatup phase, a nuclear power calibration and preconditioning phase, shutdown and flux wire replacement, a second loop heatup prior to the power burst, and the transient power burst. A single power burst of about 60 ms in duration was performed, resulting in a total fuel pellet radially averaged adiabatic energy of 240 cal/g at the axial power peak and a radial average peak fuel enthalpy of 185 cal/g. A description of the test design and conduct is given in Appendix A. (All of the appendices to this report are provided on microfiche attached to the inside of the back cover.)

Test RIA 1-2 was conducted using four individually shrouded fuel rods that had been previously irradiated to a burnup of about 4800 MWd/t. Two of the rods (Rods 802-2 and 802-4) were opened and pressurized to about 2.4 MPa to simulate end-of-life rod internal pressure. Rod 802-1 was opened, instrumented, and backfilled to a rod internal pressure of 0.105 MPa. Rod 802-3 was not opened or instrumented. The rod pretest characterization data are presented in Appendix B.

This report presents an analysis, interpretation, and discussion of the results from Test RIA 1-2. Reference 8 presents the experimental data from this test. The calculated rod behavior is presented, as well as the experiment thermal and mechanical response, including the coolant behavior, cladding temperatures, and rod internal pressure. A discussion of the failure threshold and failure modes of preirradiated fuel rods and the effect of high and

Table 1. Power Burst Facility RIA tests[a]

Test[a]	Number of Rods	Fuel Rod Type	Burnup (MWd/t)	Fuel Material	Pellet Density (%)	Pellet Outside Diameter (mm)	Diametral Gap (mm)	Axial Peak, Radial Average Fuel Enthalpy (cal/g)	Objectives and Comments
RIA-ST-1	1	PWR	0	UO_2	94	8.23	0.190	185, 250[c]	Scoping tests (ST) to
RIA-ST-2	1	PWR	0	UO_2	94	8.23	0.190	260[c]	address potential problem
RIA-ST-3	1	PWR	0	UO_2	94	8.23	0.190	225[c]	areas in the performance
RIA-ST-4	1	PWR	0	UO_2	93	9.3	0.210	350[c]	of the PBF RIA Series 1 tests. (Test RIA-ST-1 was performed as two separate power bursts.)
RIA 1-1	2	Saxton[b]	5500	UO_2	94	8.58	0.165	285[c]	To provide a comparison of irradiated and
	2	Saxton	0	UO_2	94	8.53	0.165	285[c]	unirradiated fuel behavior using Saxton rods at the NRC licensing criteria enthalpy limit of 280 cal/g UO_2.
RIA 1-2	4	Saxton	4800	UO_2	94	8.58	0.165	185[c]	To test irradiated Saxton rods at the expected fuel enthalpy to cause cladding failure. Two rods will be pressurized to BWR end-of-life conditions.
RIA 1-3	4	BWR/6	5000 to 12 000	UO_2	95	10.57	0.228	220[d]	To test preirradiated BWR/6 fuel rods at a peak fuel enthalpy of 220 cal/g.
RIA 1-4	9	Saxton	5300	UO_2	94	8.58	0.165	280[c]	To investigate core coolability of clustered, preirradiated Saxton rods for comparison with results of Test RIA 1-1.
RIA 1-6	4	BWR/6	0 to 20 000	UO_2	95	10.57	0.228	240[d]	To test preirradiated BWR/6 rods at a higher peak fuel enthalpy for comparison with the results of Test RIA 1-3.

4

Table 1. (continued)

Test[a]	Number of Rods	Fuel Rod Type	Burnup (MWd/t)	Fuel Material	Pellet Density (%)	Pellet Outside Diameter (mm)	Diametral Gap (mm)	Axial Peak, Radial Average Fuel Enthalpy (cal/g)	Objectives and Comments
RIA 1-7	9	BWR/6	0 to 12 000	UO_2	95	10.57	0.228	165[d]	To investigate the failure threshold of a cluster of preirradiated BWR/6 fuel rods.

a. All tests in this series will be performed from BWR hot-startup conditions.

b. The Saxton reactor was a small, prototype, closed cycle, pressurized, light water reactor designed by Westinghouse Electric Corporation for the USAEC.

c. Actual result of tests.

d. Enthalpy may be changed.

low rod internal pressure on rod deformation are presented, and the conclusions from this experiment are discussed.

A discussion of the PBF design and capabilities is given in Appendix C and the energy deposition measurements and postirradiation examination results are discussed in Appendices D and E, respectively. Appendix F lists the computer code used to calculate the cladding temperatures (WIZARD code) from the observed oxidation of the cladding.

TEST PREDICTIONS

Fuel rod and coolant conditions for Test RIA 1-2 were analyzed pretest using computer codes to establish a probable sequence of events during the transient. The RELAP4 computer code[9,a] was used to perform the thermal-hydraulic analysis. The RELAP4 analysis produced a tape of the coolant conditions that were used as boundary conditions for the FRAP-T5[10,b] fuel behavior code calculations. The predicted coolant behavior and the results of the FRAP-T5 analysis of the fuel rod behavior are presented in the following sections.

Coolant Behavior

The rapid heating of the coolant during an RIA event results in large perturbations in the coolant flow. The rod power at the axial peak location (0.384 m), the calculated outlet coolant pressure,

a. RELAP4/MOD5, Idaho National Engineering Laboratory Configuration Control Number H003301B.

b. FRAP-T5, Idaho National Engineering Laboratory Configuration Control Number H001183B.

and both the inlet and outlet coolant mass flux during the first 500 ms of Test RIA 1-2 are shown in Figure 2. The direct moderator heating due to the burst causes an initial pressure increase to 6.5 MPa at the outlet during the power burst and causes both the inlet and outlet flows to initially increase. This is followed by a 100-ms interval during which the pressure oscillates and the inlet and outlet flows decrease to their initial values. At 130 ms, the coolant at the 0.79-m elevation reaches saturation and begins vapor formation. The large volume generated by the vapor causes a second pressure increase to 6.55 MPa and forces the coolant out both ends of the flow shroud, increasing the outlet flow and decreasing the inlet flow. Approximately 6% of the coolant is expelled from the flow shroud, causing the outlet flow to recover by decreasing flow, and the inlet flow to increase.

The calculated outlet coolant pressure, inlet and outlet coolant mass flux, and the peak node surface heat flux during the first 25 s are shown in Figure 3. The flows and pressure remain fairly
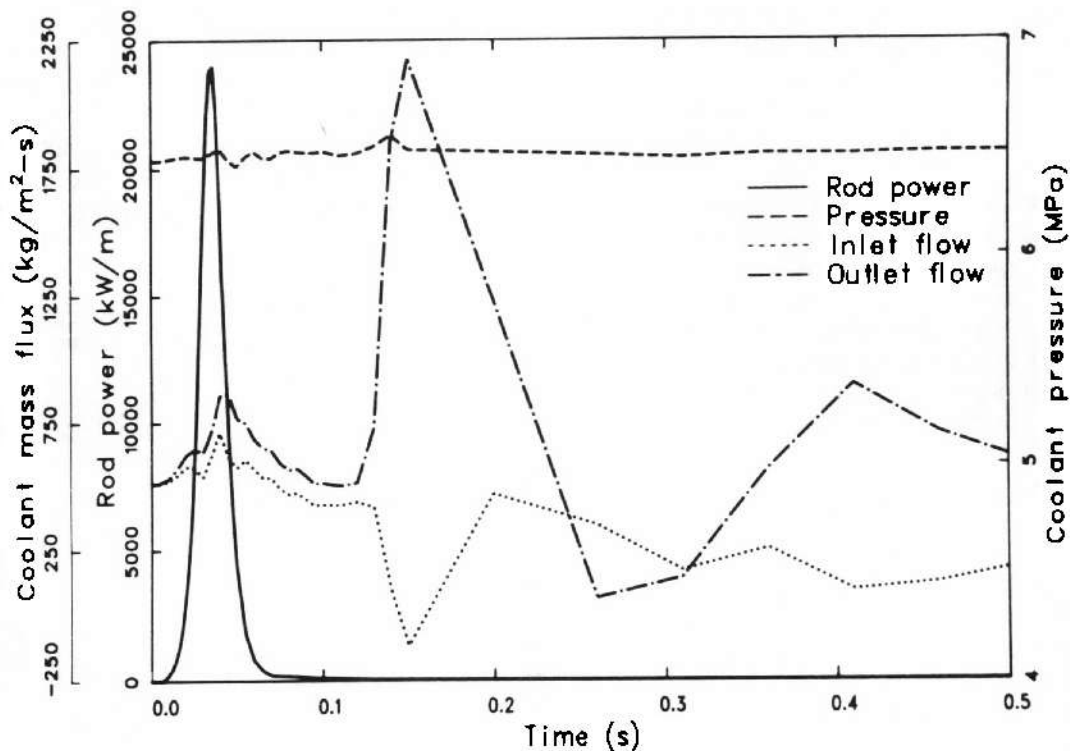
Figure 2.   Comparison of calculated rod power, coolant outlet pressure, and coolant inlet and outlet mass flux with time.

7
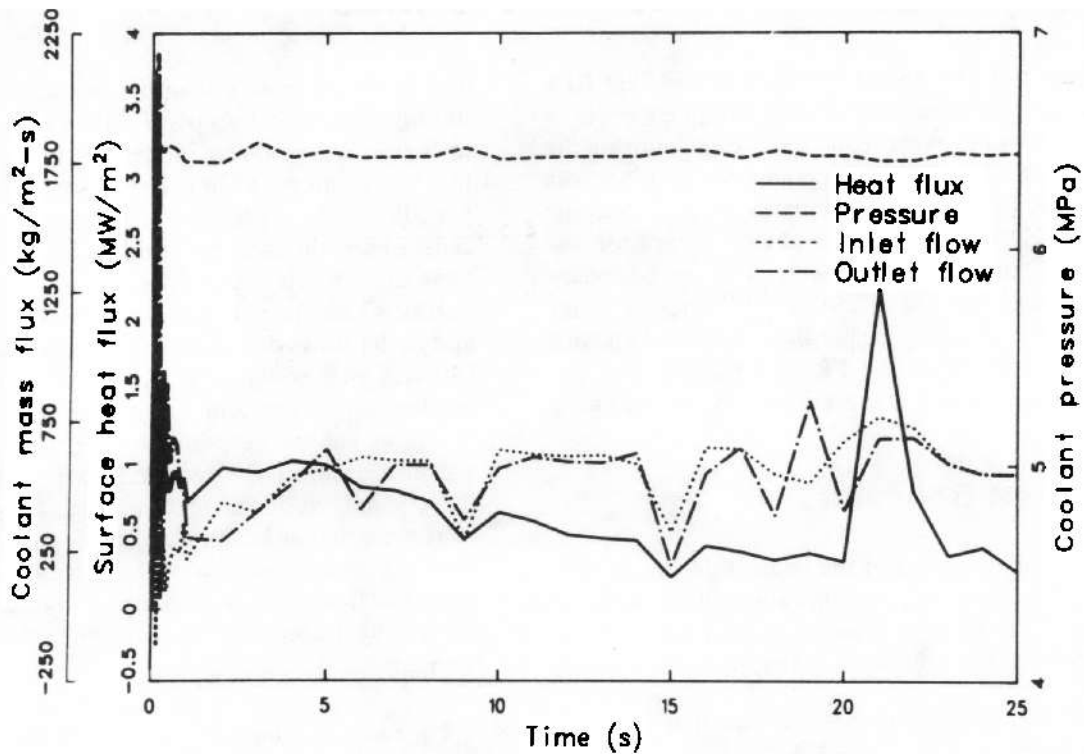
Figure 3. Comparison of inlet and outlet coolant mass flux, outlet pressure, and peak surface heat flux with time.

constant after 1 s, with the exception of perturbations at 3, 6, 9, 15, and 19 s corresponding to the large peaks in both quality and surface heat flux at those times. These peaks are believed to be code generated due to various heat slabs dropping out of film boiling.

The fuel rod heat transfer regime changes from subcooled forced convection to nucleate boiling at 36 ms, to transition boiling at 40 ms, and to stable film boiling at 65 ms, although the coolant does not reach saturation temperature until 130 ms. The axial peak node remains in film boiling until 22 s, resulting in a calculated oxide layer thickness of 32 μm and a Xi layer[a] thickness of 83 μm.

Fuel Rod Behavior

The FRAP-T5 calculated fuel centerline, fuel surface, and cladding surface temperatures at the axial peak flux location during the first 120 ms and the first 25 s of the Test RIA 1-2 transient are plotted in Figures 4 and 5. The test rod power as a

function of time is also presented in Figure 4. Figure 6 presents the radial temperature distribution across the fuel at the peak flux location at given times between 34 ms and 5 s. A linear peak power of 24 200 kW/m occurs at 35 ms. The fuel heats up much faster than the cladding and the fuel peak temperatures are initially located near the fuel surface. The fuel surface temperature
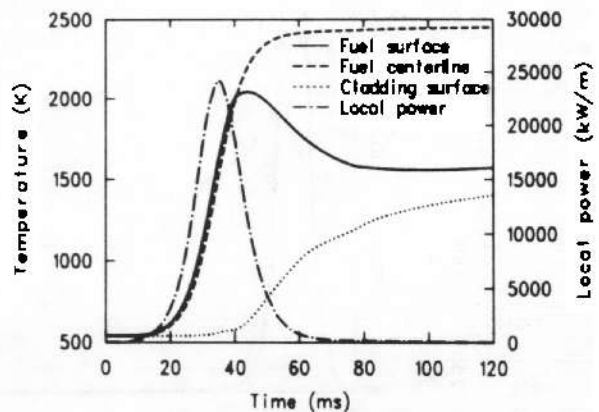
Figure 4. Fuel centerline, fuel surface, and cladding surface temperatures, and rod power during the first 120 ms of Test RIA 1-2.

a. The Xi layer is the combination of the oxide and alpha-zircaloy layers.

8
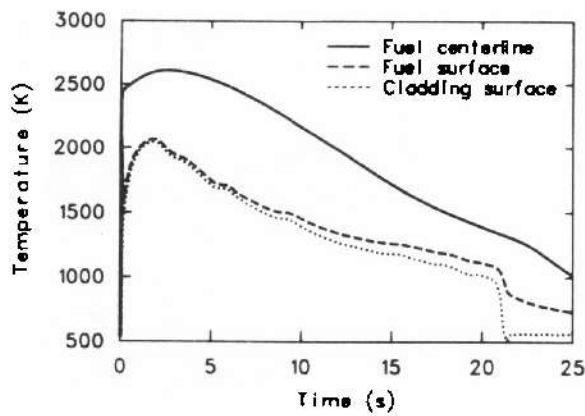
Figure 5.   Fuel centerline, fuel surface, and cladding surface temperatures during the first 25 s of Test RIA 1-2.
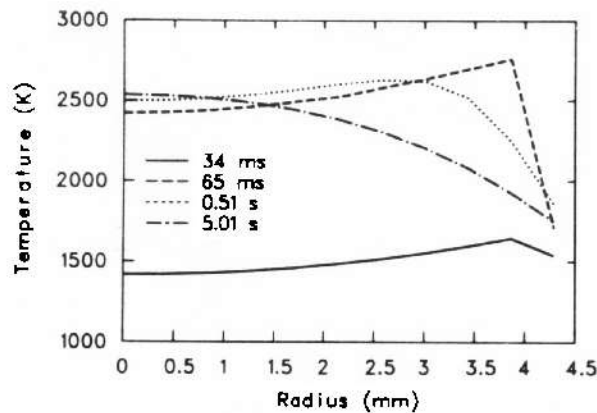
Figure 6.   Fuel radial temperature distribution at the axial peak power location at various times during Test RIA 1-2.

reaches a peak value of approximately 2040 K at 44 ms and then decreases about 500 K during the next 40 ms due to increased heat transfer to the cladding resulting from gap closure. The fuel

centerline temperature rapidly increases to approximately 2400 K by 60 ms and then continues to increase more slowly for about 3 s. A fuel peak temperature of 2765 K occurs at a point near the fuel surface at 60 ms. As the fuel radial temperature distribution changes with time, the fuel surface and cladding temperatures reach maximum values of 2060 and 2045 K, respectively, at approximately 2 s, and the fuel centerline temperature peaks at 2606 K at 3 s. On the basis of the predicted fuel temperatures, fuel melting would not be expected during Test RIA 1-2.

The rod power, fuel-cladding structural gap, and cladding stress and strain during the first 200 ms of the transient for Rod 802-2, a high pressure rod, are plotted in Figure 7. The figure shows that the rapid increase in fuel temperature while the cladding remains cool causes the fuel to expand faster than the cladding, resulting in closure of the fuel-cladding gap shortly after peak power (35 ms). With the closing of the fuel-cladding gap, there is a rapid increase in cladding stress as the fuel expands against the cladding, with rod failure predicted to occur at 46 ms for the high pressure rods.

Figure 8 shows the rod power, structural gap, and cladding stress and strain for Rod 802-3, a low pressure rod, during the first 400 ms of the transient. As in the high pressure rods, the differential thermal expansion of the hot fuel against the cold cladding causes the fuel-cladding gap to close during the burst, resulting in a large stress peak at gap closure. Unlike Rod 802-2, FRAP does not calculate failure of Rod 802-3 during the stress peak, but the cladding is expected to strain as it warms up. The effective plastic strain increases to 3.5% at 310 ms, at which time an instability in the elastic strain model forces the code to predict failure.
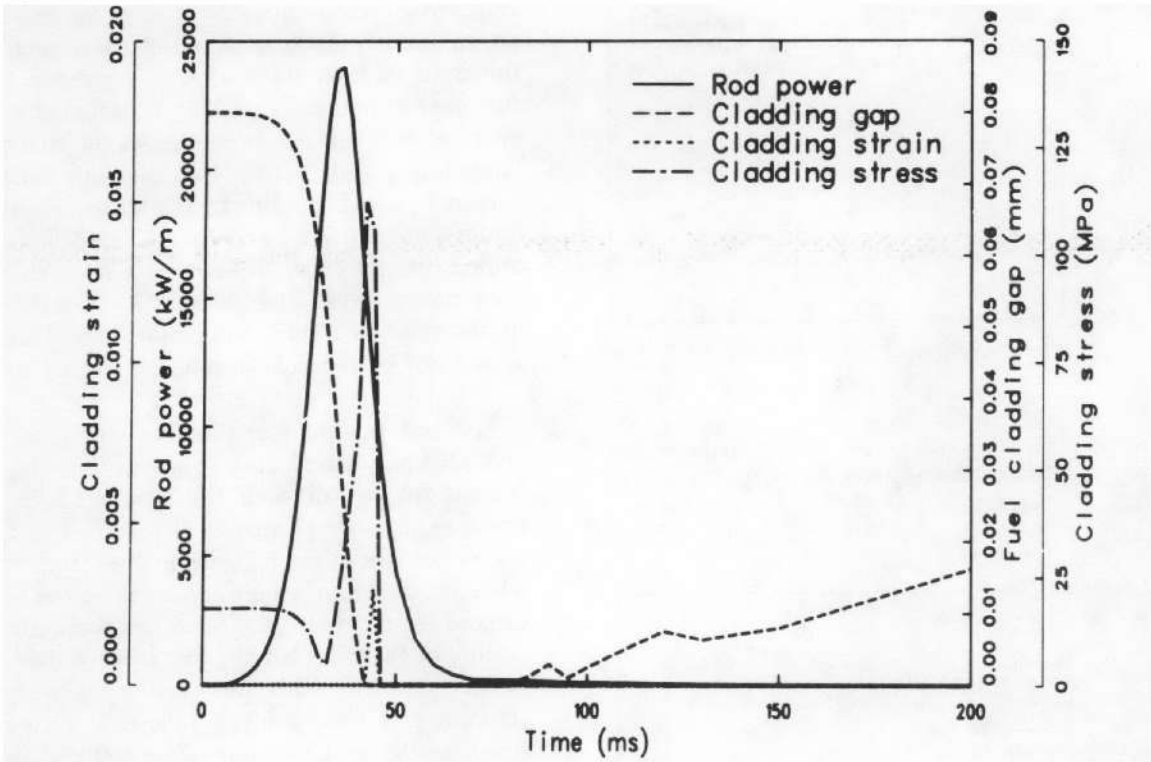
Figure 7.   Comparison of rod power, fuel-cladding gap, and cladding stress and strain with time for Rod 802-2.
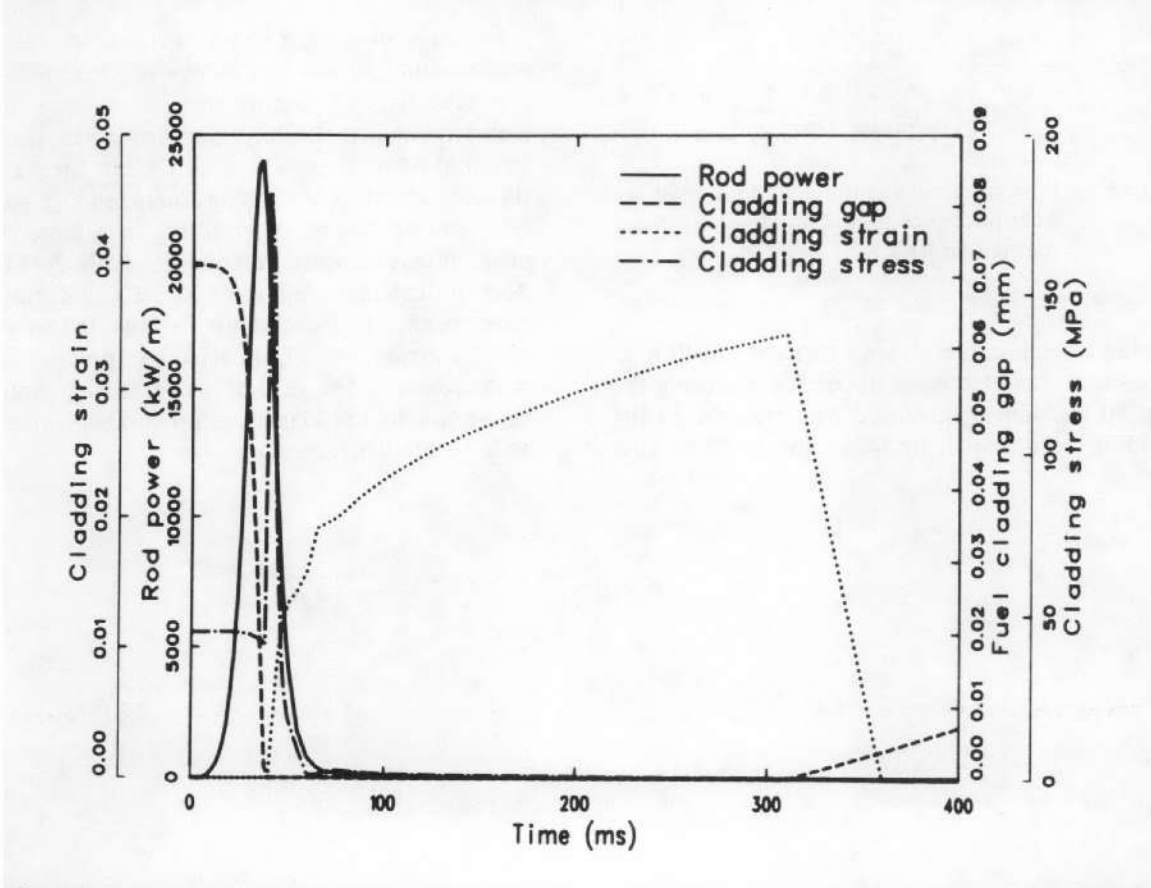
Figure 8.   Comparison of rod power, fuel-cladding gap, and cladding stress and strain with time for Rod 802-3.

EXPERIMENT THERMAL AND MECHNICAL RESPONSE

The fuel rods and shrouds of Test RIA 1-2 were instrumented so that the thermal and mechanical response of the fuel rods and coolant could be determined during the test. This section presents the analysis of the on-line data. All of the plots from the instrumentation are presented in Reference 8.

Coolant Behavior

The coolant behavior during Test RIA 1-2 was determined by the flow shroud instrumentation for each fuel rod. Each rod was instrumented with an inlet, outlet, and differiential temperature (ΔT) thermocouples, along with an inlet flowmeter and a pressure transducer at the outlet of the flow shroud.

Coolant Flow. The flowmeters used in Test RIA 1-2 were unidirectional instruments, thus not allowing direct measurement of flow reversal. However, by looking at the change of phase of the ac response, the flow reversal and recovery to

positive flow could be estimated, and is shown for Rod 802-1 along with the RELAP4 calculated coolant flow in Figure 9.

In general, all four flowmeters exhibited similar responses to the burst. A sharp flow reversal occurred at approximately 10 ms after peak power, with recovery to positive (upward) flow occurring within 150 ms after peak power. The flow reversal is believed to be due to direct heating of the coolant during the power burst, resulting in a volume of high pressure causing flow reversal at the inlet. Integrating the flow response shows that 15% of the initial coolant volume in the shroud was expelled during the burst.

Figure 9 shows a discrepancy between the calculated and measured flow rates. Instead of reversing flow at the inlet during the burst, the calculations predicted an increase in inlet flow. The predicted inlet flow increase is probably due to higher moderator heating in the downcomer region as compared to the moderator heating in the flow shroud. The predictions also indicated
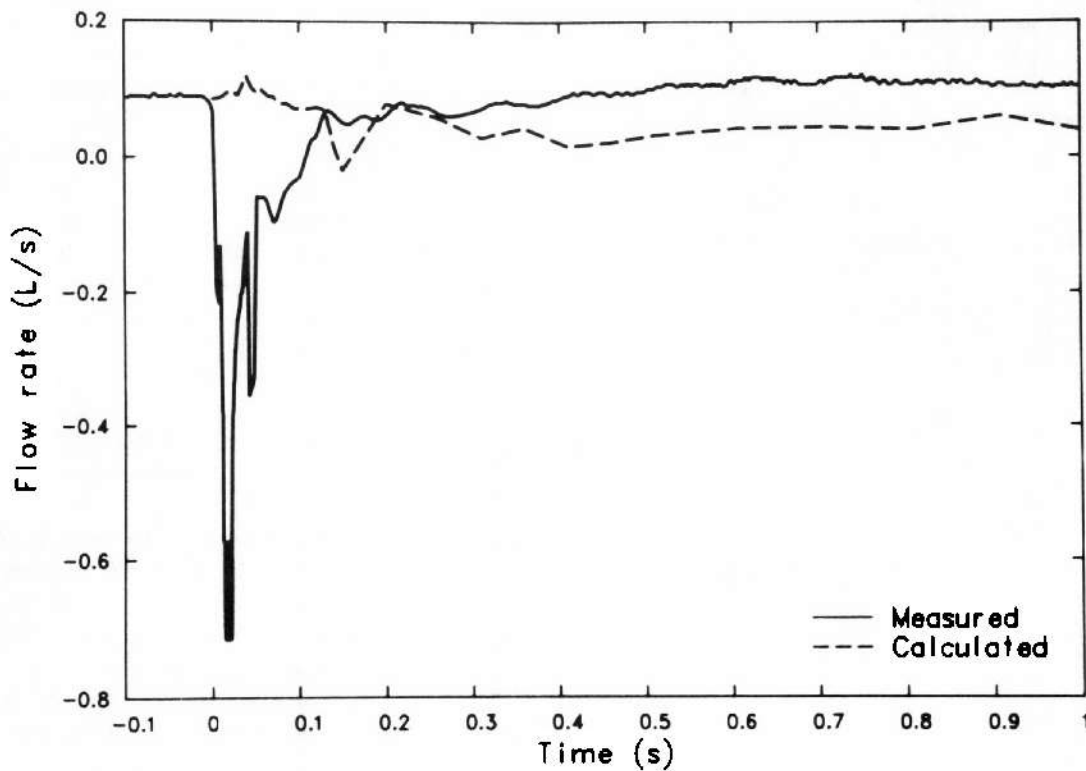
Figure 9.   Rod 802-1 measured and calculated coolant flow rate.

that flow reversal would occur when the coolant reached saturation, but the flowmeter did not show this, indicating that the upstream pressure drop was larger than modeled by the RELAP4 code.

Coolant Pressure. The outlet shroud pressure response for all rods is shown in Figures 10 and 11. Figure 11 also shows the predicted coolant pressure for comparison. The initial pressure increase peak ranged from 7.1 to 7.2 MPa approximately 17 ms after peak power. The initial pressure increase was followed by a much broader pressure increase 400 to 500 ms later, with a peak of 6.8 MPa. The second pressure increase slowly decayed (~1.5 to 2.0 s) to a relatively constant pressure of 6.5 MPa, which lasted for approximately 9 s. This was followed by a decrease in pressure to a minimum of 6.3 MPa, occurring at
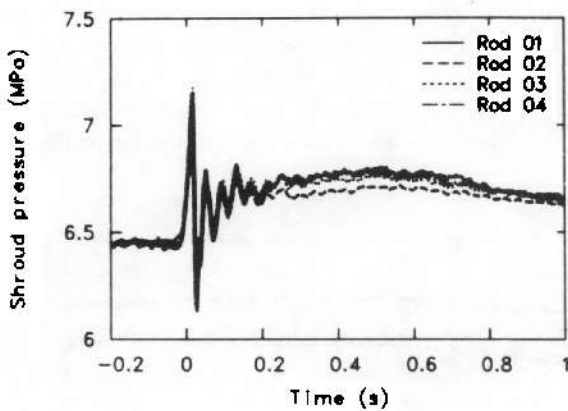
Figure 10.   Measured coolant pressures for 1 s.
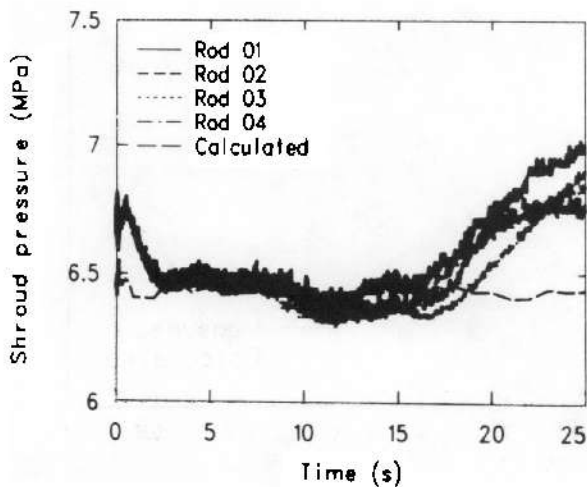
Figure 11.   Measured and calculated coolant pressures for 25 s.

10 s, and followed by a third and much broader and higher pressure increase to 7.2 MPa at 30 s, before decreasing to the preburst pressure of 6.45 MPa at 60 s. The period between 3 and 15 s corresponds closely to the estimated time in film boiling; however, the reason for the increase in pressure that precedes quench is not apparent. The mechanism for the second pressure pulse that occurred between 0.5 and 3 s was probably due to the bulk coolant attaining saturation conditions.

The calculated coolant pressure response did not follow the measured pressure response very well, as shown in Figure 11. The calculated pressure remained fairly constant throughout the test. RELAP did not predict any of the three pressure increases and decreases measured by all four pressure transducers. The pressure sensors are somewhat sensitive to temperature gradients. However, the outlet temperature is relatively constant, as shown in Figure 12, and, therefore, the pressure increase between 16 and 30 s shown in Figure 11 may be real.

Coolant Temperature. Each flow shroud in Test RIA 1-2 was instrumented with inlet, outlet, and ΔT thermocouples. The pressure response for each flow shroud was used to calculate the saturation temperature of the coolant with time. By comparing the measured outlet and ΔT responses with the calculated saturation temperature, an estimate of the time that a two-phase mixture of coolant existed in the flow shrouds can be made. Figure 12 shows the outlet thermocouple response, the addition of the inlet and ΔT thermocouple responses, and the calculated saturation temperature with time, along with the shroud pressure for Rod 802-1. The other three rods provided similar data. The plot shows that a two-phase mixture was exiting the flow shrouds between 1 and about 19 s. These times correspond to the pressure decrease after the second pulse and the pressure increase during the third pulse.

The estimated time in film boiling obtained from the outlet coolant thermocouples agrees reasonably well with the film boiling time obtained from cladding surface temperature calculations described in the next section. In general, the cladding thermocouples indicated film boiling times approximately 5 s shorter than the calculated values. The shorter film boiling time obtained from the cladding surface thermocouples may be due to premature quenching of the thermocouples.

12
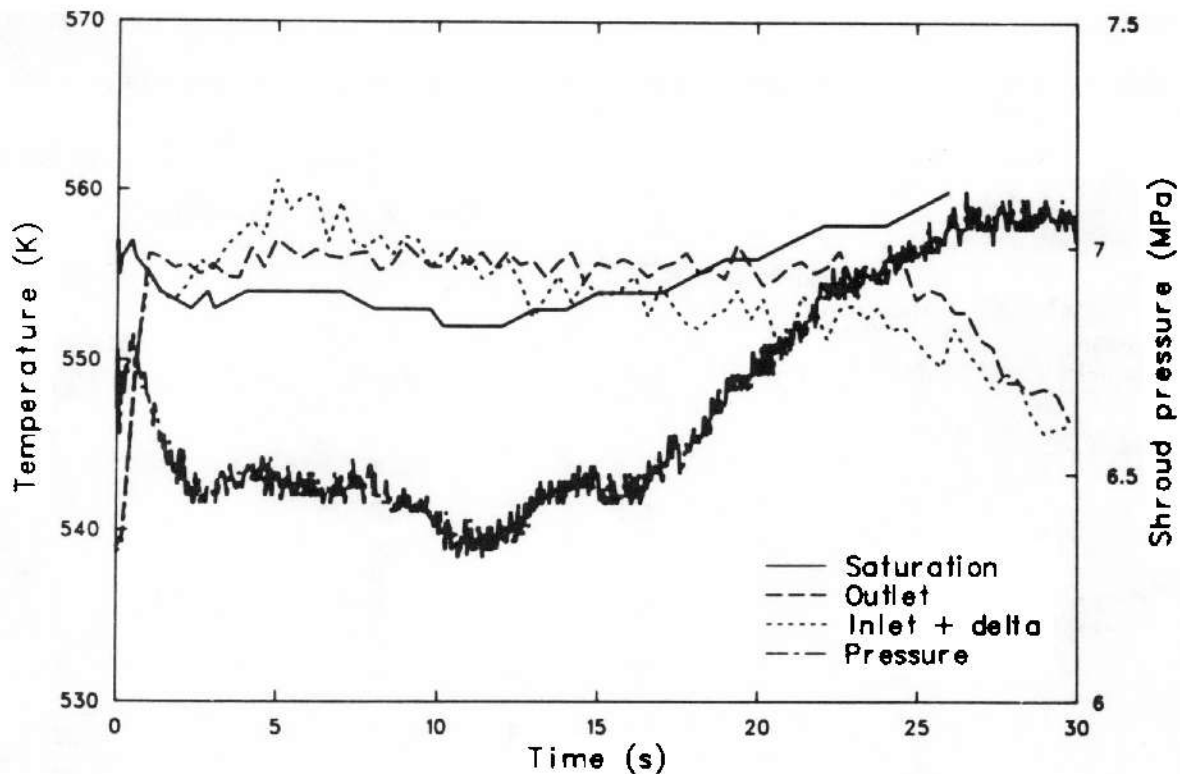
Figure 12. Measured coolant outlet temperature, shroud pressure, and calculated saturation temperature for Rod 802-1.

Fuel Rod Behavior

The fuel rod cladding temperature and the rod internal pressure were measured during Test RIA 1-2 by two cladding surface thermocouples on each of Rods 802-1 and 802-2, and internal pressure transducers on Rods 802-1, 802-2, and 802-4. This section characterizes the cladding temperatures using several techniques in addition to the thermocouple measurements, provides alternate methods of confirming the peak temperatures attained, and presents the rod internal pressures.

Cladding Temperatures. The cladding temperatures were determined by (a) metallographic examination of the cladding and ZrO_2 layer microstructure, (b) measured oxide layer thicknesses, (c) thermocouple data from the test, and (d) FRAP-T5 computer code calculations. This section describes the temperatures estimated by each of these methods.

Examination of the cladding microstructures provided a rough estimate of the peak temperatures at which the cladding operated during the test. The four, broad temperature ranges that can

be characterized by microstructural changes are (a) as-fabricated, stress relieved zircaloy at $T < 920$ K; (b) equiaxed alpha zircaloy at $920 < T < 1105$ K; (c) two-phase mixture of alpha and beta zircaloy at $1105 < T < 1245$; and (d) beta zircaloy for $1245 < T < T_{melting}$.

Table 2 lists the observed microstructures from the metallographic mounts for the rods in Test RIA 1-2. All four rods exhibited beta zircaloy microstructures in the central portion of the rods, indicating cladding surface temperatures greater than 1245 K and alpha plus beta to beta structures at the top end of the rods, indicating cladding surface temperatures probably between 1200 and 1300 K. Representative photographs of the observed cladding microstructures are shown in Appendix E.

A variation of the COBILD computer code,[9] called WIZARD, was used to estimate the cladding surface peak temperatures from the measured oxide thicknesses (Appendix F). The oxide and oxygen-stabilized alpha-zircaloy $[\alpha(O)Zr]$ layer thicknesses, along with the total oxygen uptake, are calculated using a parabolic rate equation. The oxidation rates were determined by

13

Table 2. Cladding microstructure and measured ZrO_2 and oxygen-stabilized alpha-zircaloy layers

| Elevation[a] (cm) [Sample] | Observed Microstructure | | Measured Layer Thicknesses (μm) | | | | |
	Cladding	Oxide[b]	α-Zr(O) Inner	α-Zr(O) Outer	ZrO_2 Inner	ZrO_2 Outer	Measured α-Zr(O)/ZrO$_2$
Rod 802-1							
	β	S	12	6	0	6	1.00
	β	S	8	5	0	6	0.83
14	β	S	7	4	0	4	1.00
[M-12]	β	S	11	8	0	5	1.60
	β	S	7	4	0	6	0.67
	β	S	10	5	0	6	0.83
	β	S	8	11	0	9	1.22
	β	S	0	13	0	10	1.30
29	β	S	0	10	0	9	1.11
[M-13]	β	S/D	8	15	0	11	1.36
	β	S	0	12	0	11	1.09
	β	S	11	11	0	9	1.22
	β	D	6	9	0	8	1.12
	β	D	10	8	0	7.4	1.08
45	β	D	6	11	0	9.4	1.17
[M-1]	β	D	10	11	0	9	1.22
	β	D	1(	12	0	11	1.09
	β		11	9	0	9	1.00
52[c]	β	D	0	12	0	10	1.20
[M-2]	β	D	5	14		10	1.40
	β	S	9	11	0	9	1.22
	β	S	10	9	0	7	1.29
61	β	S	0	15	0	10	1.50
[M-14]	β	S	7	13	0	11	1.18
	β	S	0	13	0	11	1.18
	β	S	11	12	0	11	1.09
	β	S	0	3	0	3.4	0.88
	β	S	0	3	0	4	0.75
76	β	S	0	6	0	5	1.20
[M-15]	β	S	7	3	0	4	0.75
	β	S	7	1	0	4	0.25
	β	S	0	0	0	0	—

Table 2. (continued)

Elevation[a] (cm) [Sample]	Observed Microstructure		Measured Layer Thicknesses (μm)				Measured α-Zr(O)/ZrO$_2$
			α-Zr(O)		ZrO$_2$		
	Cladding	Oxide[b]	Inner	Outer	Inner	Outer	
Rod 802-2							
33 [M-18]	β	D	0	12	0	10	1.20
	β	D	11	0	0	8	0.0
	β	D	0	9	0	9	1.00
45 [M-4]	β	D	13	7	0	7	1.00
	β	D	0	5	0	6	0.83
	β	D	9	5	0	6	0.83
	β	D	0	6	0	6	1.00
	Low $\beta \rightarrow \beta$	D	0	11	0	9	1.22
52[c] [M-5]	Low $\beta \rightarrow \beta$	D	0	9	0	6	1.50
	Low $\beta \rightarrow \beta$	D	5	4	0	7	0.57
	Low $\beta \rightarrow \beta$	—	2	3	0	0	—
	$\alpha + \beta \rightarrow \beta$	S	0	0	0	3	0.00
	$\alpha + \beta \rightarrow \beta$	S	2	2	0	2	1.00
78 [M-6]	$\alpha + \beta \rightarrow \beta$	S	2.4	1	0	2	0.50
	$\alpha + \beta \rightarrow \beta$	—	0	0	0	0	0.00
	$\alpha + \beta \rightarrow \beta$	—	2	2	0	0	—
	$\alpha + \beta \rightarrow \beta$	S	2	1.2	0	2	0.60
Rod 802-3							
	β	S/D	8	22	17	14	1.57
38 [M-20]	β	S/D	6	22	14	13	1.69
	β	S/D	7	16	13	12	1.33
	β	D	16	14	0	11	1.27
	β	D	7	16	0	9	1.78
45 [M-7]	β	D	17	15	0	10	1.50
	β	S/D	10	15	0	10	1.50
	β	D	5	15	0	10	1.50
	β	D	14	15	0	10	1.50
	β	D	3	15	8	12	1.25
	β	D	7	13	2	10	1.30
48[c] [M-8]	β	D	7	19	7	13	1.46
	β	D	5	18	18	12	1.50
	β	S/D	10	19	15	16	1.19
	β	S/D	10	22	18	12	1.83

Table 2. (continued)

Elevation[a] (cm) [Sample]	Observed Microstructure		Measured Layer Thicknesses (μm)				Measured α-Zr(O)/ZrO$_2$
			α-Zr(O)		ZrO$_2$		
	Cladding	Oxide[b]	Inner	Outer	Inner	Outer	
Rod 802-3 (continued)							
	β	D	5	13	0	12	1.08
60	β	S/D	9	14	0	10	1.40
[M-9]	β	D	7	15	6	10	1.50
	β	S/D	13	13	6	9	1.44
	β	S/D	12	13	11	10	1.30
67	β	S/D	8	6	8	6	1.00
[M-16]	β	D	10	9	11	9	1.00
	β	D	6	11	17	8	1.38
Rod 802-4							
31 [M-19]	β	S/D	8	12	0	8	1.50
	β	D	0	8	0	8	1.00
45	β	S/D	7	6	0	6	1.00
[M-10]	β	S	9	8	0	8	1.00
	β	S/D	0	7	0	7	1.00
47[c]	Low β	D	4	7	0	7	1.00
[M-11]	Low β	S/D	0	6	0	6	1.00
	Low β	S/D	8	11	0	7	1.57
	Low β	S	7	6	0	6	1.00

a. Several orientations were measured at each elevation from the bottom of the fuel stack.

b. S = single oxide layer, D = duplex oxide layer.

c. Longitudinal sample.

Cathcart from isothermal test measurements.[12] The code requires a temperature-time history to be input and varies the magnitude of the profiles until the measured layer thicknesses are obtained. The estimated temperature uncertainty due to photographic magnification and measurement uncertainties of the oxide and oxygen-stabilized alpha layers is 80 K. The measured oxygen-stabilized alpha zircaloy and oxide layer thicknesses are listed in Table 2.

The temperature dependence of the growth rates of the oxide (ZrO_2) and oxygen-stabilized alpha layers are sufficiently different above 1460 K that a rough estimate of the peak temperature can be made by taking the ratio of the two layers and using the Cathcart correlations. The measured ratios are listed in Table 2. The occurrence of a single or duplex oxide layer structure can also indicate cladding peak temperatures[13] and is discussed in Appendix F.

Rods 802-1 and 802-2 were instrumented with cladding surface thermocouples at the 46- and 79-cm locations on both rods. Rods 802-3 and 802-4 did not have cladding surface thermocouples. Cladding temperatures were calculated for the locations corresponding to the metallurgical mounts using the FRAP-T5 computer code. The estimated peak uncertainty for the FRAP-T5 calculated temperatures is 70 K. The thermocouple measured and FRAP-T5 calculated time-temperature profiles were adjusted in magnitude to produce the measured oxide layer thicknesses at the thermocouple locations by the WIZARD calculation. The unadjusted and adjusted thermocouple measured and FRAP-T5 calculated time-temperature profiles for the 46- and 79-cm elevations of Rods 802-1 and 802-2 are plotted in Figures 13 through 16. The adjusted cladding peak temperatures are listed in Table 3. The thermocouples measured only the thermocouple temperature, whereas the FRAP-T5 code calculated the cladding surface temperature near the thermocouples. Corrections were made to the thermocouple measured temperatures for fin cooling effects by using the COUPLE computer code.[a] The COUPLE analysis is presented in Appendix F. The COUPLE adjusted thermocouple temperatures agree with the FRAP-T5 calculated temperatures that were adjusted to produce the measured oxide layer thicknesses.

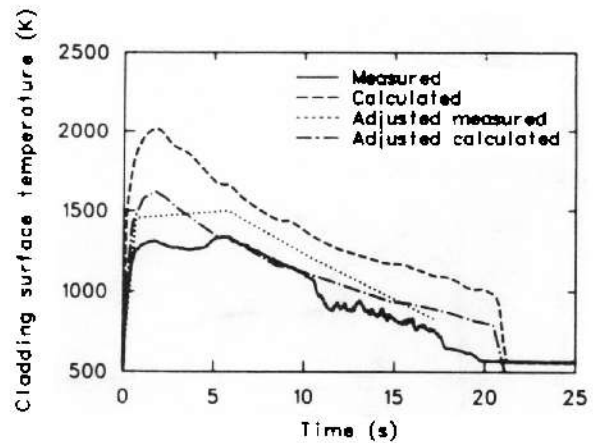a. COUPLE/MOD3, Idaho National Engineering Laboratory Configuration Control Number C0018001.

Figure 13. Thermocouple measured and FRAP calculated, and adjusted thermocouple measured and FRAP calculated cladding surface temperatures at 0.46 m on Rod 802-1.

Figure 14. Thermocouple measured and FRAP calculated, and adjusted thermocouple measured and FRAP calculated cladding surface temperatures at 0.79 m on Rod 802-1.

The WIZARD adjusted thermocouple profiles result in a cladding surface peak temperature that is in very good agreement (< 5 K) with the WIZARD adjusted FRAP-T5 calculated temperature profiles at the 79-cm location of both Rods 802-1 and 802-2, and the 46-cm location of Rod 802-2. A large difference in the calculated cladding surface peak temperatures from the two types of profiles is shown at the 46-cm location of Rod 802-1. The large difference can be explained by comparing the FRAP-T5 calculated and thermocouple measured temperature profiles shown in Figure 13. The FRAP temperature profile shows a rapid temperature increase followed by a slow

Figure 15. Thermocouple measured and FRAP calculated, and adjusted thermocouple measured and FRAP calculated cladding surface temperatures at 0.46 m on Rod 802-2.
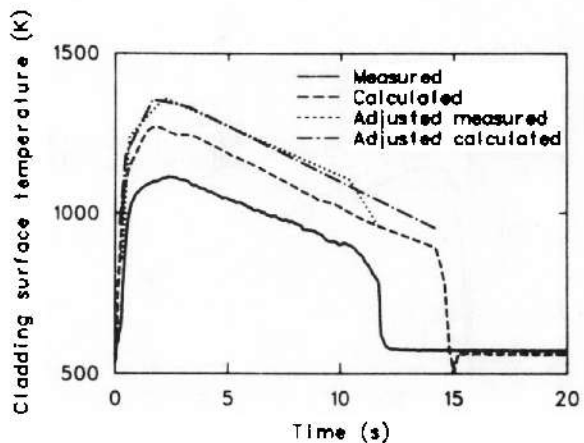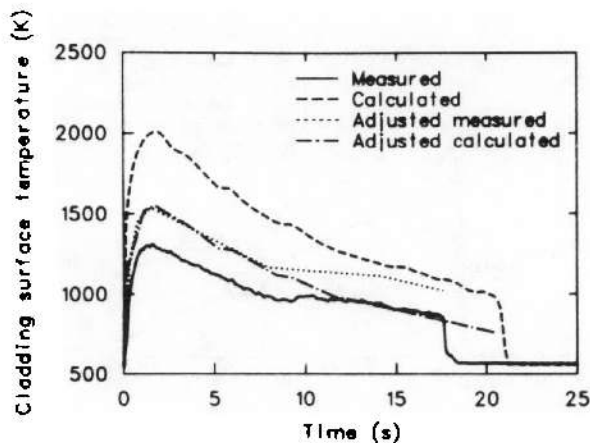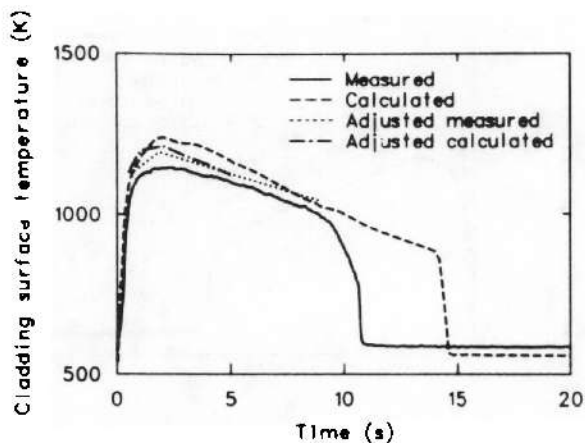

Figure 16. Thermocouple measured and FRAP calculated, and adjusted thermocouple measured and FRAP calculated cladding surface temperatures at 0.79 m on Rod 802-2.

temperature decrease, with rapid quench and rewet at 22 s. The thermocouple response also shows a rapid temperature increase, but is followed by approximately 5 s of relatively constant temperature before decreasing. Since the oxide layer thickness is a function of both time and temperature, the thermocouple profile results in a lower peak temperature than the FRAP-T5 profile because it is less peaked in shape.

Figure 17 shows the axial variation along Rod 802-1 of the FRAP-T5 calculated and the FRAP-T5 oxide adjusted cladding surface peak temperature. The FRAP-T5 axial peak tempera-

ture profile was adjusted to give the same peak temperature as the FRAP-T5 oxide adjusted temperature at the 29-cm location. As shown in the figure, the FRAP-T5 profile has a cosine shaped distribution with a maximum at the axial power peak, whereas the profile adjusted to the oxide thickness has a much flatter distribution over the length of the rod, with a slight dip near the 46-cm thermocouple location. The dip may be due to the presence of the thermocouple, but no conclusions can be reached since the temperature dip (~ 20 K) is well within the uncertainty of the oxidation model (~ 80 K). The relatively flat axial temperature profile calculated using the oxide measurements is significantly different from the FRAP-T5 calculated axial profile. This effect was also observed in the other three rods. Since the cladding surface temperature is, to a large extent, dependent on the surrounding coolant conditions, the large difference in the axial profiles indicates that the thermal-hydraulic boundary conditions supplied to FRAP-T5 by the RELAP4 code may not be applicable to the actual experiment.

Oxide layer thickness measurements were taken at various circumferential locations for each transverse metallographic mount from all four rods to estimate the circumferential temperature variation. The circumferential deviation was on the order of 40 K, which is less than the 80-K uncertainty resulting from the oxide measurements; therefore, no significant circumferential temperature variation was found.

Rod 802-3 failed during the burst, and posttest examinations showed 22 longitudinal cracks on the rod. The metallographic samples prepared from the rod were clustered between the axial flux peak and the 67-cm location. The FRAP-T5 profiles were adjusted downward 100 to 300 K to match the observed oxide measurements. Rod 802-3 had the highest peak temperatures (1740 K) during the test, which may be related to the lower coolant flow measured in the rod flow shroud during the test.

The two high pressure rods (802-2 and 802-4) experienced cladding surface peak temperatures approximately 100 K lower than the two low pressure rods (802-1 and 802-3), probably as a direct result of the observed 5 to 6% diametral strains, and were 1640 and 1580 K, respectively.

Rod Internal Pressure. Pressure transducers were installed in the upper plenum of Rods 802-1,

Table 3. Adjusted cladding temperatures

Elevation[a] (cm) [Sample]	Adjusted FRAP-T5 Calculated Profile		Adjusted Thermocouple Profile	
	Peak Temperature (K)	Average[b] Peak Temperature (K)	Peak Temperature (K)	Average[b] Peak Temperature (K)
Rod 802-1				
14 [M-12]	1480 1480 1390 1440 1480 1480	1460 (40)		
29 [M-13]	1610 1640 1610 1670 1670 1610	1640 (30)		
45 [M-1]	1590 1560 1630 1620 1670 1620	1610 (30)	1490 1470 1530 1520 1570 1520	1520 (30)
52[c] [M-2]	1640 1640	1640		
61 [M-14]	1580 1510 1610 1630 1630 1630	1600 (50)		
76 [M-15]	1320 1360 1400 1360 1360	1360 (30)	1320 1360 1410 1360 1360	1360 (30)
Rod 802-2				
33 [M-18]	1640	1640		

19

Table 3. (continued)

Elevation[a] (cm) [Sample]	Adjusted FRAP-T5 Calculated Profile		Adjusted Thermocouple Profile	
	Peak Temperature (K)	Average[b] Peak Temperature (K)	Peak Temperature (K)	Average[b] Peak Temperature (K)
Rod 802-2 (continued)				
45 [M-4]	1580 1620 1550 1510 1510 1510	1550 (40)	1570 1600 1540 1500 1500 1500	1540 (40)
52[c] [M-5]	1590 1480 1520	1530 (50)		
78 [M-6]	1310 1210 1210 1210	1240 (50)	1290 1190 1190 1190	1220 (50)
Rod 802-3				
38 [M-20]	1740 1720 1690	1720 (20)		
45 [M-7]	1670 1610 1640 1640 1640 1640	1640 (20)		
48[c] [M-8]	1690 1640 1720 1690 1780 1690	1700 (50)		
60 [M-9]	1660 1610 1610 1580	1610 (30)		

20

Table 3. (continued)

Elevation[a] (cm) [Sample]	Adjusted FRAP-T5 Calculated Profile		Adjusted Thermocouple Profile	
	Peak Temperature (K)	Average[b] Peak Temperature (K)	Peak Temperature (K)	Average[b] Peak Temperature (K)
Rod 802-3 (continued)				
67 [M-16]	1610 1480 1480 1480	1550 (60)		
Rod 802-4				
31 [M-19]	1580	1580		
45 [M-10]	1580 1510 1580 1550	1560 (40)		
47[c] [M-11]	1550 1510 1550 1510	1530 (20)		

a. Several orientations were measured at each elevation from the bottom of the fuel stack.

b. Numbers in parentheses are the standard deviation.

c. Longitudinal sample.

802-2, and 802-4. The Rod 802-1 transducer failed early in the test; therefore, no plenum pressure information was obtained from the low pressure rods. The transducers on the two high pressure rods (802-2 and 802-4) behaved similarly, and a comparison plot of the transducer response of Rod 802-2 and the FRAP-T5 calculated plenum pressure is shown in Figure 18 for the first 25 s of the test. Figure 19 plots the same variables for the first 100 ms.

Several factors influence the rod internal pressure during an RIA transient. The tempera-

ture increase, gap closure, and fission product release all tend to increase rod internal pressure, whereas cladding expansion decreases rod internal pressure.

The FRAP-T5 calculation predicted that the high pressure rods would fail early in the transient, resulting in the code forcing the rod internal pressure to equilibrate with the coolant pressure. Figure 19 shows the calculated rod pressure to be below the coolant pressure at the start of the transient and then increasing during the burst as the fuel heats up and the available gas volume
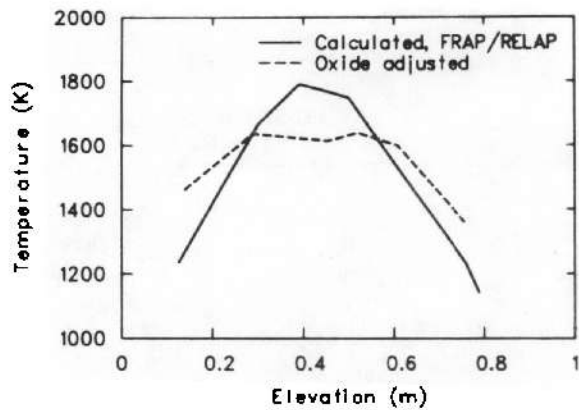
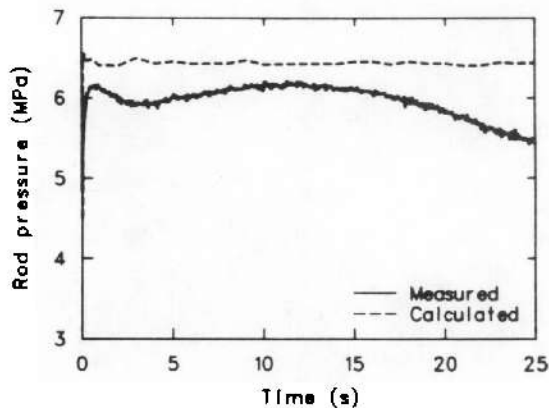Figure 17. Axial variation of cladding peak temperatures on Rod 802-1.

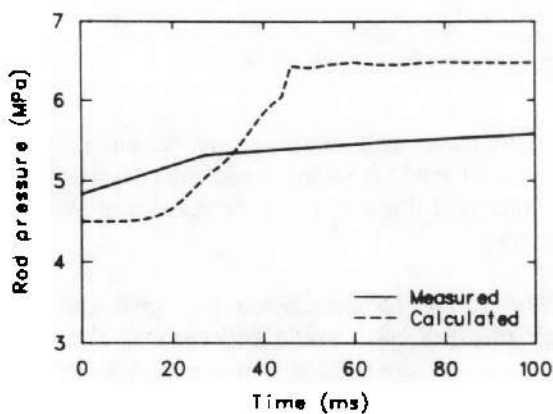Figure 18. Measured and calculated rod internal pressure of Rod 802-2 for 25 s.

Figure 19. Measured and calculated rod internal pressure of Rod 802-2 for 100 ms.

decreases due to the closing of the fuel-cladding gap. The sharp jump in rod pressure between 44 and 46 ms is due to the code-predicted failure of the rod at 46 ms, which resulted in the rod pressure following the RELAP4 calculated coolant pressure for the remainder of the transient (Figure 18). The measured internal pressure in the figures was adjusted (to remove an offset in the measurement) to 4.62 MPa at the start of the transient to match the calculated pressure based on calculated gap temperature and void volume and internal pressure measured prior to the test. The measured pressure shows two increases during the test, with the first increase of about 0.5 MPa occurring at 2 s, followed by a much broader increase of approximately 0.5 MPa that peaked at 12 s. The significant feature of the transducer response is that it remained below the coolant pressure throughout the transient and, since post-test measurements showed positive strains in the middle of the rod instead of collapse, the transducer response indicates that the rod plenum was probably isolated from the heated section of the rod for some period of time during the transient.

A second analysis was performed using the cladding surface temperature estimates from the previous section and assuming the internal pressure was equal over the length of the rod. A comparison of the transducer response and the calculated response is shown in Figure 20. The calculated plenum pressure response shown in Figure 20 represents an upper bound on plenum pressure. The internal pressure was assumed to be equal over the length of the rod to prevent false failure prediction at the hot region of the rod due
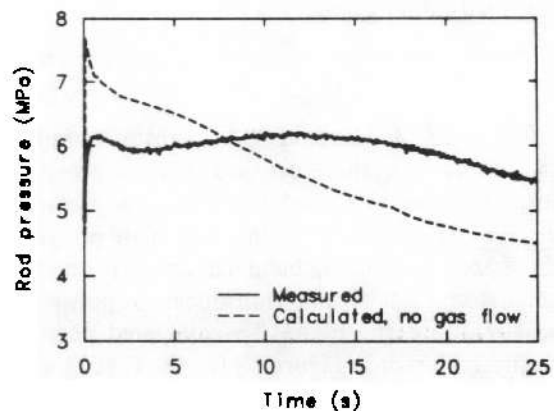

Figure 20. Measured and FRAP-T6 calculated rod internal pressure of Rod 802-2.

to high internal pressures and subsequent pressure equilibration of the rod with the coolant. As expected, the measured pressure remained below the calculated pressure during the first 8 s of the test, but increased above the calculated values for the remainder of the test. The low measured pressure during the first 8 s could be due to the isolation of the upper plenum from the heated section of the rod caused by the fuel-cladding gap closure. The first pressure increase recorded by the transducer may be due to the temperature increase of the gas in the plenum region. The slow rise in pressure that starts at about 3 s may be an indication that the plenum was equilibrating with the rest of the fuel rod very slowly. The decrease in pressure that occurs between 1 and 3 s corresponds to the time when the rods were believed to have deformed, although this should not have been reflected in the partially isolated plenum, since the plenum was still in the process of equilibrating up to the pressure of the rest of the rod. The higher than expected plenum pressure measured after 8 s does not seem reasonable since the calculated plenum pressure represents an upper bound in the plenum, as mentioned above. Also, since the calculated deformation of the rod was less than actually measured, the available volume was larger; therefore, the measured pressure should have been even lower. One possible explanation for the measured response could be due to a temperature gradient effect on the transducer, which has been seen in other PBF tests using the same type of transducers. However, no gradient is expected during an RIA test since the transducer remained in a single-phase fluid throughout the test.

FAILURE THRESHOLD OF PREIRRADIATED FUEL RODS

The purpose of the RIA Test Series is to determine the failure threshold for fuel rods during a hypothetical reactivity initiated accident. The results of the earlier work obtained in the Special Power Excursion Reactor Tests and in the Japanese Nuclear Safety Research Reactor were reviewed in the introduction to this report. This section summarizes the previous RIA failure threshold data, discusses the failure threshold in light of the Test RIA 1-2 results, describes in detail the failure of the one RIA 1-2 rod, and discusses possible failure modes.

Failure Threshold

In general, from previous RIA tests, the failure threshold of unirradiated fuel rods was found to be in the range of 205 to 225 cal/g axial peak, radial average fuel enthalpy (260 to 265 cal/g peak fuel enthalpy near the fuel surface). Prepressurization of NSRR fuel rods to internal pressures greater than 1.2 MPa reduced the failure threshold of unirradiated fuel rods to about 150 cal/g axial peak, radial average fuel enthalpy. The tests previously conducted during the present RIA test series, the RIA Scoping Tests, indicated a failure threshold for previously unirradiated fuel rods of about 240 cal/g axial peak, radial average fuel enthalpy, slightly higher than the previous data.[14,15]

The unirradiated SPERT rods tested at energy depositions slightly above the failure threshold appeared to have failed as a result of melting and then cracking of the oxygen embrittled cladding upon cooldown. Eleven tests were conducted using previously irradiated rods during the SPERT-CDC tests. The lowest energy deposition rod failure observed was in CDC Test 756 (143 cal/g axial peak, radial average fuel enthalpy and previously irradiated to 32.7 GWd/t). The rod failure was one small (< 1 cm), axial cladding split. In the test conducted with the next higher enthalpy insertion, Test 859 (154 cal/g axial peak, radial average fuel enthalpy and previously irradiated to 31.8 GWd/t), the failure comprised three long, axial cladding splits, which together extended over most of the active length of the rod, and one ruptured blister.[16]

Cladding failure in the PBF RIA Scoping Tests was due to plastic flow of the cladding, producing regions of cladding wall thickening and thinning. The zircaloy was then oxidized by steam and UO_2, and became completely embrittled in the thinner regions. Extensive cracking of the embrittled cladding occurred due to thermal stresses during the quench and rewet following about 30 s of film boiling. After the occurrence of extensive fuel shattering along grain boundaries in the two fuel rods tested at axial peak, radial average fuel enthalpies of 250 and 260 cal/g (275 to 290 cal/g UO_2 radial peak near the pellet surface), approximately 10 and 15% of the UO_2 fuel, respectively, was swept out of the flow shrouds.[14]

The four fuel rods used in Test RIA 1-2 were subjected to a radially averaged peak fuel enthalpy of 185 cal/g (215 cal/g peak enthalpy near the fuel surface). Three of the four fuel rods did not fail. One of the low pressure rods, 802-3, remained relatively intact, but failed by means of 22 small (< 1 cm long), longitudinal cracks starting at about 14.5 cm and extending to about 68.1 cm from the bottom of the 91-cm-long fuel stack. Table 4 presents the location of the cladding cracks. The radial average peak fuel enthalpy at the 14.5- and 68.1-cm locations was about 140 cal/g. The other three rods experienced cladding deformation, which is discussed in a subsequent section. The failure threshold (140 cal/g UO_2) of previously irradiated rods, as determined from the energy deposition at the lowest axial position where cracks were found on the one failed rod from Test RIA 1-2, is generally consistent with earlier SPERT results for previously irradiated fuel rods.

The differences between the four fuel rods, and especially between the two low pressure rods, that would result in only one rod failing are not apparent. The NSRR results showed that increasing the rod pressure decreases the failure threshold. Therefore, it would be expected that the high pressure rods would be more likely to fail at a given peak fuel enthalpy than a low pressure rod at the same enthalpy. Rod 802-3 failed by cladding cracking over regions of the rod at an enthalpy insertion of 140 to 185 cal/g UO_2. None of the other rods showed any cracking, although they all had regions in this same enthalpy range.

Different procedures were used for the fabrication of the four Test RIA 1-2 rods. Three of the

Table 4. Description of cracks in Rod 802-3

Crack Elevation from Bottom of Fuel Stack (cm)	Crack Description
67.9 to 68.1	2 mm long, closed, white deposit around outside
66.5 to 66.9	4 mm long, open, no deposit
63.8 to 64.3	5 mm long, closed, dark deposit around outside
62.7 to 62.8	1 mm long, closed, no deposit
60.4 to 60.6	2 mm long, slightly open, no deposit
59.8 to 60.3	5 mm long, open, dark deposit around outside
57.1 to 57.3	2 mm long, open, no deposit
55.9 to 56.1	2 mm long, closed, white deposit around outside
55.5 to 55.8	3 mm long, closed, white deposit around outside
52.2 to 52.3	1 mm long, closed, white deposit around outside
50.7 to 51.0	3 mm long, closed, white deposit around outside
50.5 to 50.7	2 mm long, open, no deposit
49.3 to 49.5	2 mm long, open, white deposit around outside
48.4 to 48.5	1 mm long, closed, slight white deposit around outside
37.9 to 38.1	2 mm long, closed, white deposit around outside
37.2 to 37.4	2 mm long, closed, white deposit around outside
36.9 to 37.3	4 mm long, open, dark deposit around outside
32.2 to 33.0	8 mm long, slightly open, dark deposit around outside
31.7 to 31.8	1 mm long, slightly open, no deposit
30.3 to 30.5	2 mm long, slightly open, no deposit
14.5 to 15.0	5 mm long, closed, white deposit around outside

rods were opened after Saxton irradiation and before PBF testing so that instrumentation could be installed. The rods were backfilled with a 77.7% helium 22.3% argon mixture. These three rods did not fail. The one rod that was not opened, Rod 802-3, failed.

The initial internal pressure of Rod 802-3 is not certain because it was not measured after Saxton irradiation. The data transmitted with the fuel rods indicated that the rod was originally air-filled at atmospheric pressure. Characterization of similar rods that had also been irradiated in the Saxton reactor showed that the rods that were initially air-filled at atmospheric pressure contained about 20% less free gas after Saxton irradiation. This may have been due to reaction of the oxygen with the cladding inside surface.

A change in rod internal chemistry may have occurred in the three rods that were opened prior to testing, which may have reduced the potential for stress-corrosion cracking in these rods. Although the mechanisms are not well understood, several elements have been considered to cause stress-corrosion cracking in zircaloy. The elements most often cited are iodine, cesium, cadmium, and tellurium.[18] All of the rods were in storage after the Saxton irradiation for more than five years before being opened. The elements previously listed are all solid at room temperature and are generally combined with other fission products or oxygen as compounds. Some iodine will sublimate at room temperature and atmospheric pressure; however, the remaining iodine would probably be combined with the cesium as CsI. It may be that the elements that can cause stress-corrosion cracking of the zircaloy were not released from the rods upon opening, but rather were oxidized when the insides of the rods were exposed to air or the impurities present in the helium-argon fill gas, so that the elements may not have been available to react with the zircaloy at high temperatures.

Characterization of Rod 802-3 Failure

The failure of Rod 802-3 was characterized by at least 22 longitudinal cracks, all less than 1 cm long and at random orientations, dispersed over the center two-thirds of the fuel rod. Several of the cracks were examined to determine the failure

mode. Cracks at the 67.2-, 49.4-, 48-, and 37-cm elevations are shown in various stages as the cracks were polished through in Figures 21 through 26. The crack at the 67.2-cm elevation (Figure 21) was wide, without the deposition on the outside surface around the crack seen at other crack locations. A transverse sample was cut at this location, mounted, and polished to show the crack in cross section. The figure shows the crack as it was ground through. In the first view, the crack is fairly straight through the wall. In Figure 21(c), there are two incipient cracks on the cladding inside surface and one on the outside surface. The oxygen-stabilized alpha zircaloy and ZrO_2 are equally as thick on the inside of the crack as they are on the outside surface of the cladding, indicating that the cladding failed at low temperature, before the rod went into film boiling. This is characteristic of all of the cracks examined. Although it appears that the cracking follows the prior beta grain boundaries, the cracks probably occurred before the beta structure was formed, and the beta grains then formed along the cracks. Zirconium dioxide has filled the incipient cracks on the inside surface of the cladding shown in Figure 21(d). The through-wall crack in this view is straighter, with rounded corners at the cladding inside and outside surface. This is probably due to the oxidation of the crack surface. The crack is branched at the inside surface in Figure 21(e), and it no longer extends through the cladding in the view shown in Figure 21(f).

The crack at 49.4 cm, shown in Figure 22, appears to join a crack from the outside surface and an irregularity on the inside surface of the cladding. Although the cracks appear to have initiated on the outside surface of the cladding, it may be that they initiated on the inside surface and propagated in the axial as well as the radial direction. The higher temperature at this location compared with the location shown in Figure 21 resulted in significantly more oxygen-stabilized alpha on the outside surface of the cladding and on the surfaces of the crack. The oxygen-stabilized alpha layer was brittle, and severe cracking of this layer is apparent in the photographs. As the sample polishing progressed, it became evident that the cladding crack was a straight, through-wall crack. In Figure 22(d), four incipient cracks are evident on the inside of the cladding.
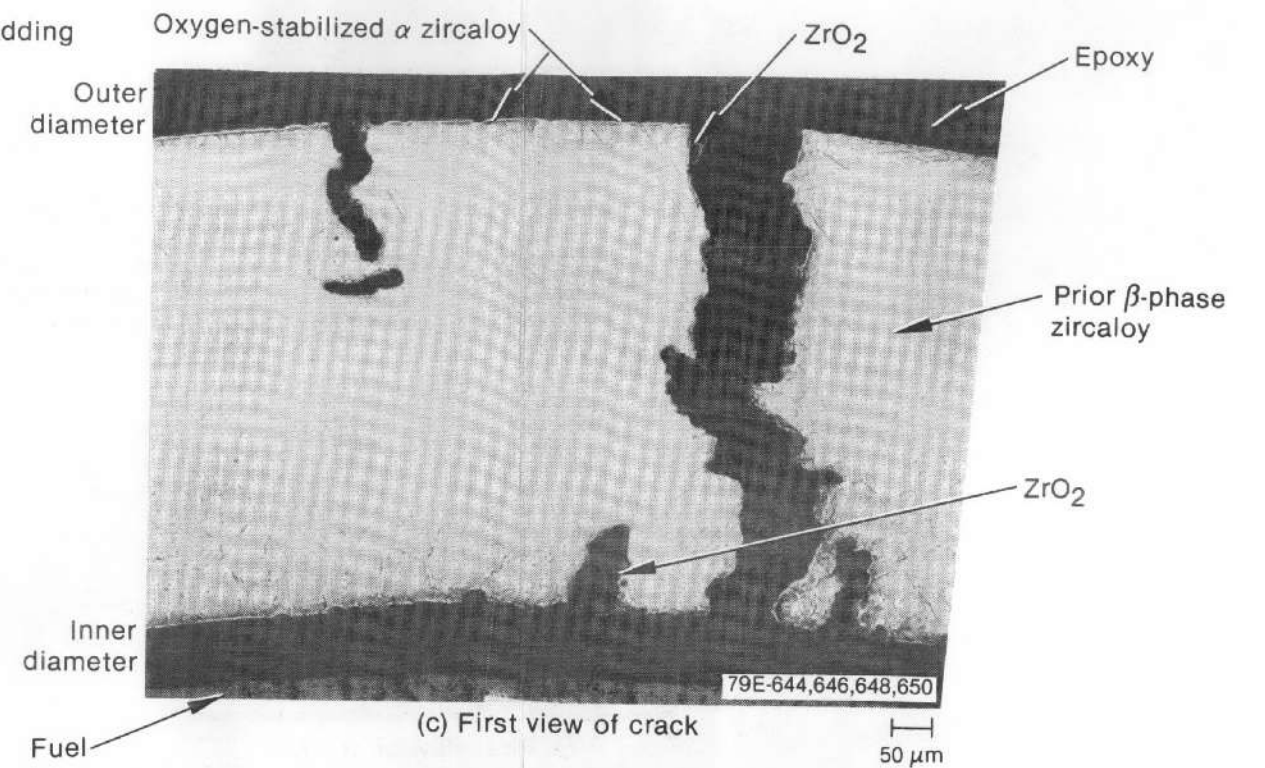
The crack shown in Figure 23 (at 48 cm) occurred at the location of a pellet-to-pellet interface, a high stress point in the cladding. The section of
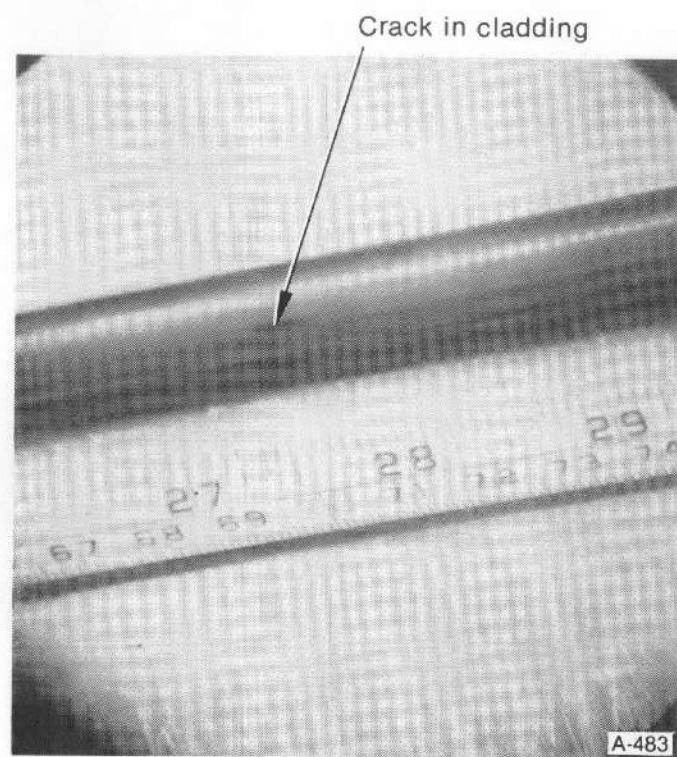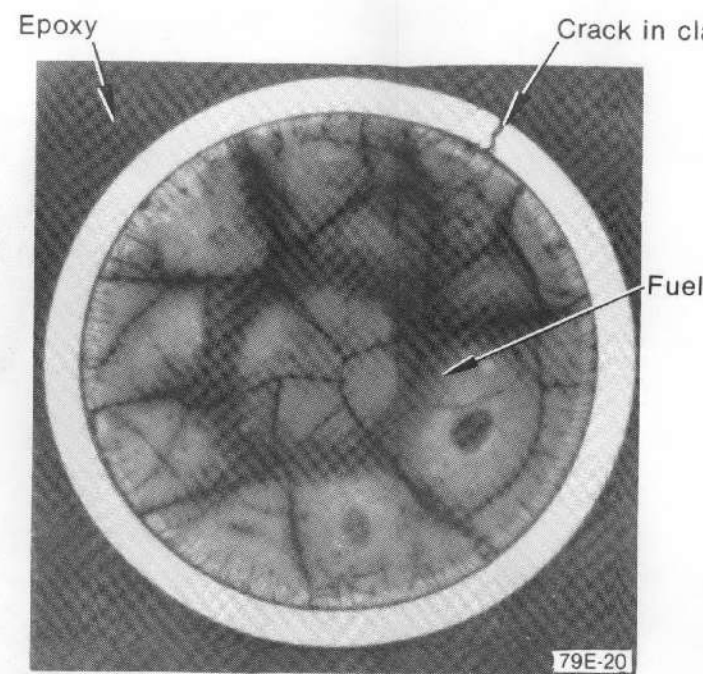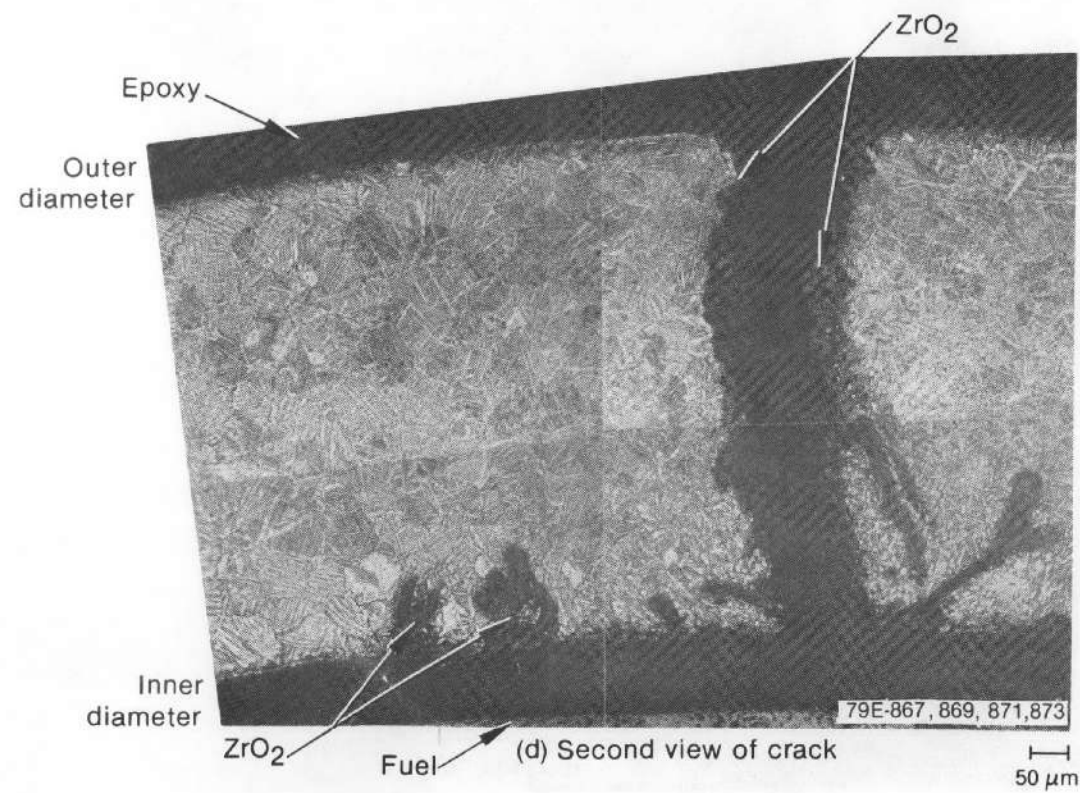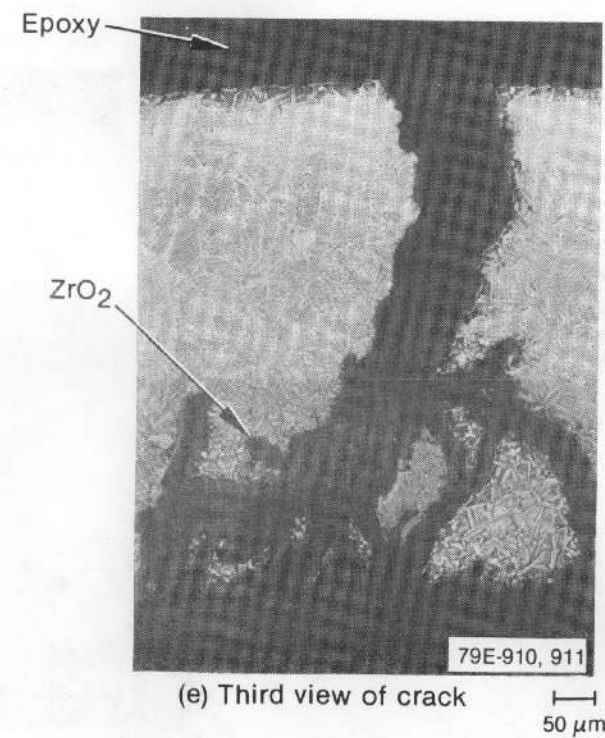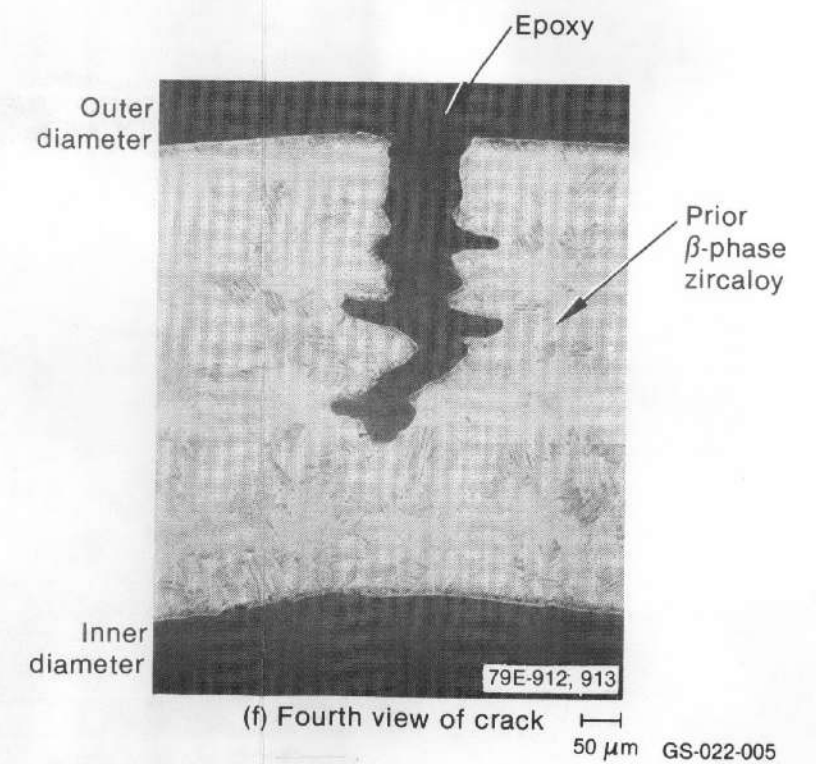
Figure 21. Crack in cladding at the 67.2-cm elevation of Rod 802-3.

(a) First view of crack — 79E-1023, 1025 — 50 μm

(b) Second view of crack — 79E-1027, 1029 — 50 μm

(c) Third view of crack — 79E-1058, 1059 — 50 μm

(d) Fourth view of crack — 79E-1061 — 1064 — 50 μm

GS-022-004
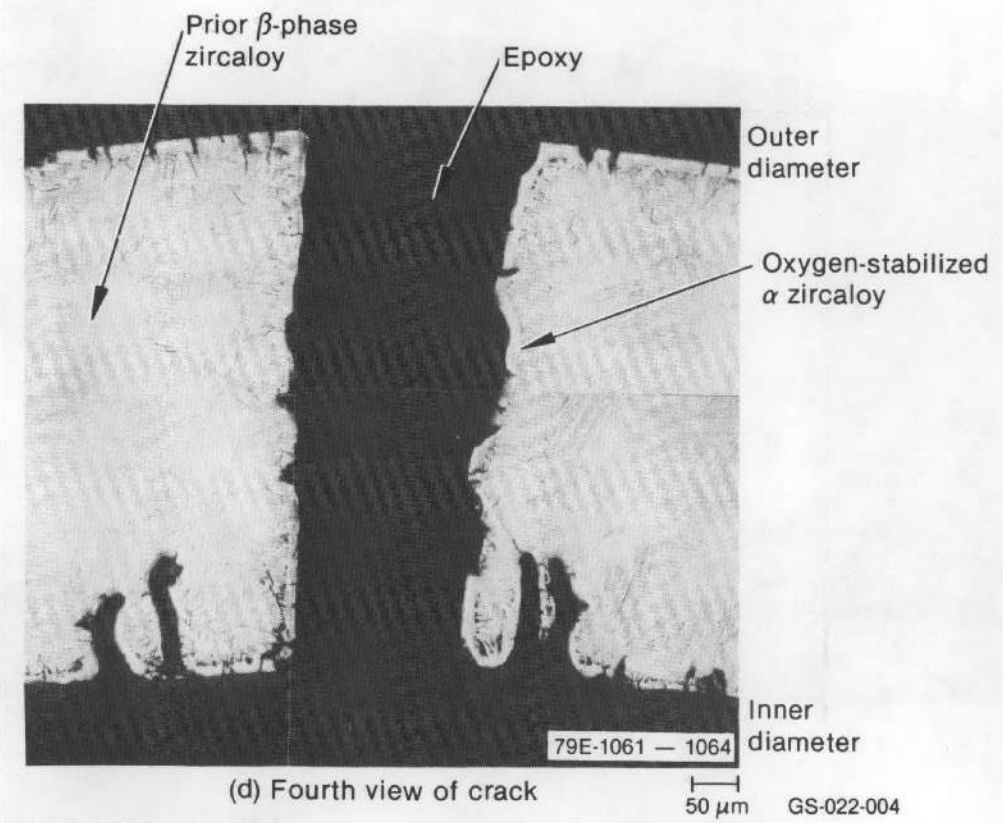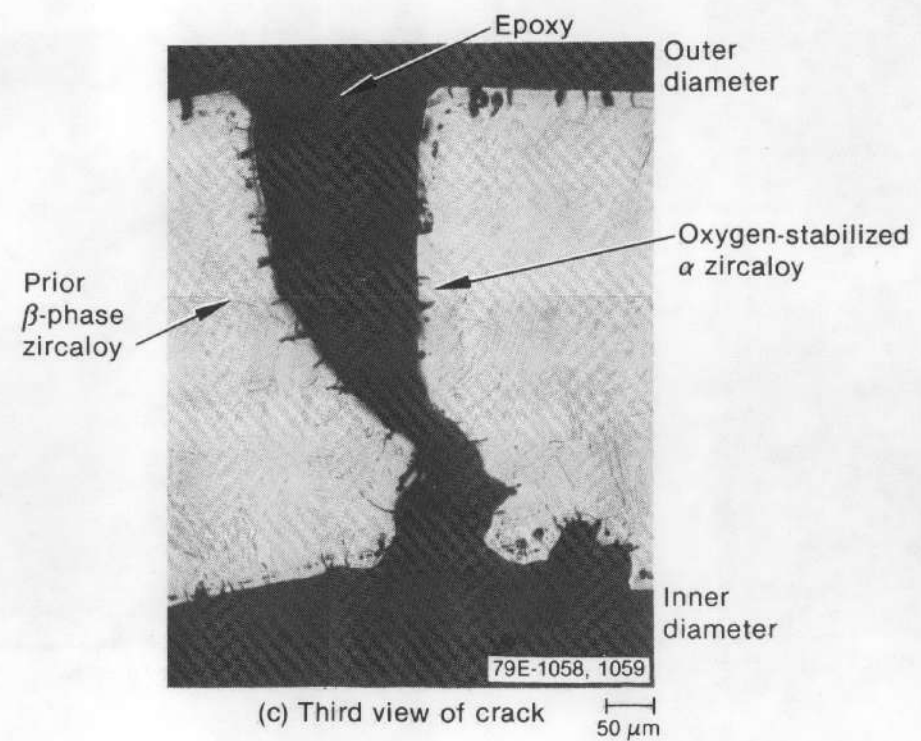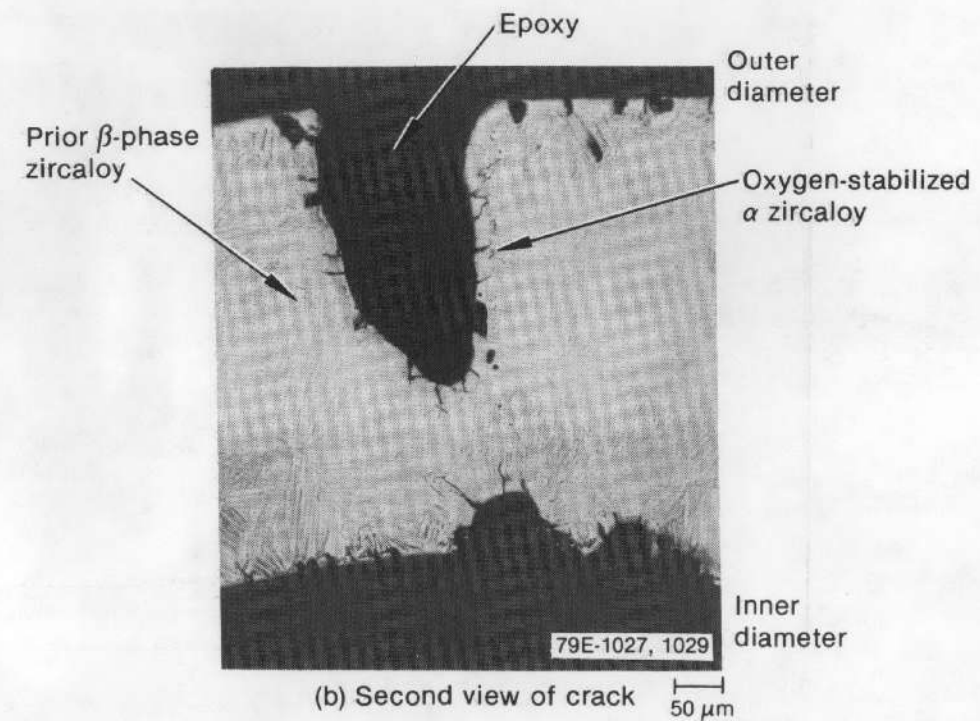
Figure 22.   Crack in cladding at the 49.4-cm elevation of Rod 802-3.

(a) Longitudinal section at crack location
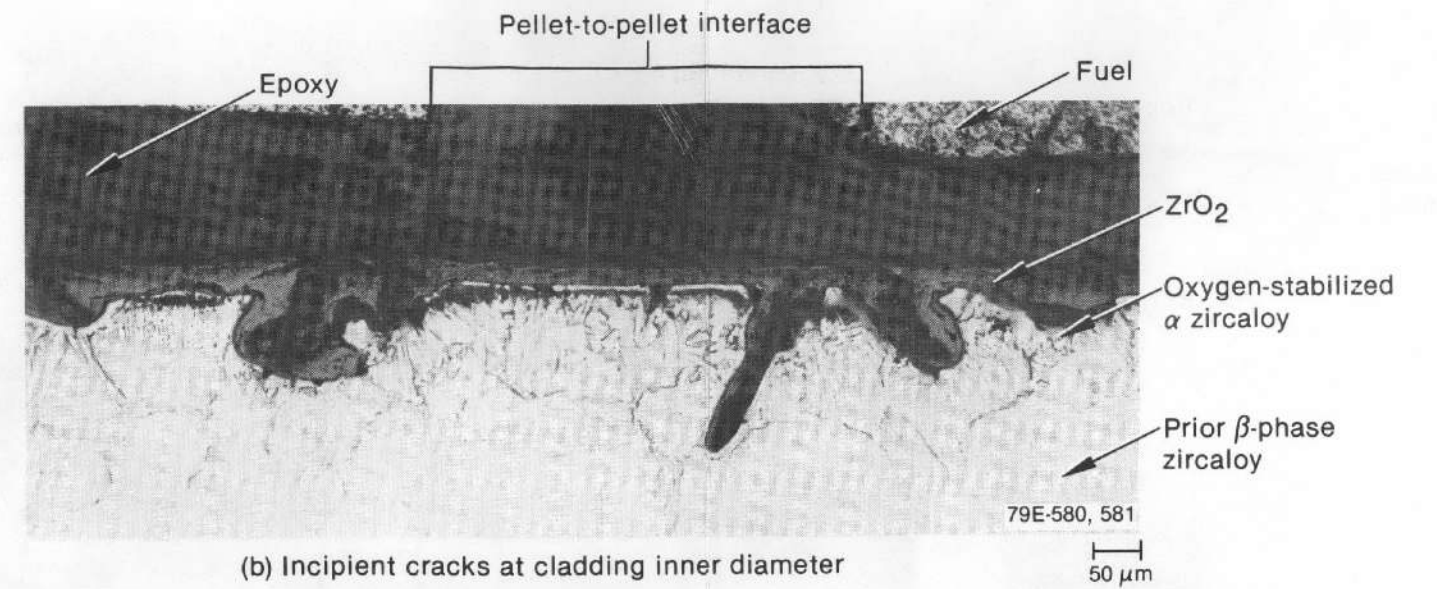
(b) Incipient cracks at cladding inner diameter
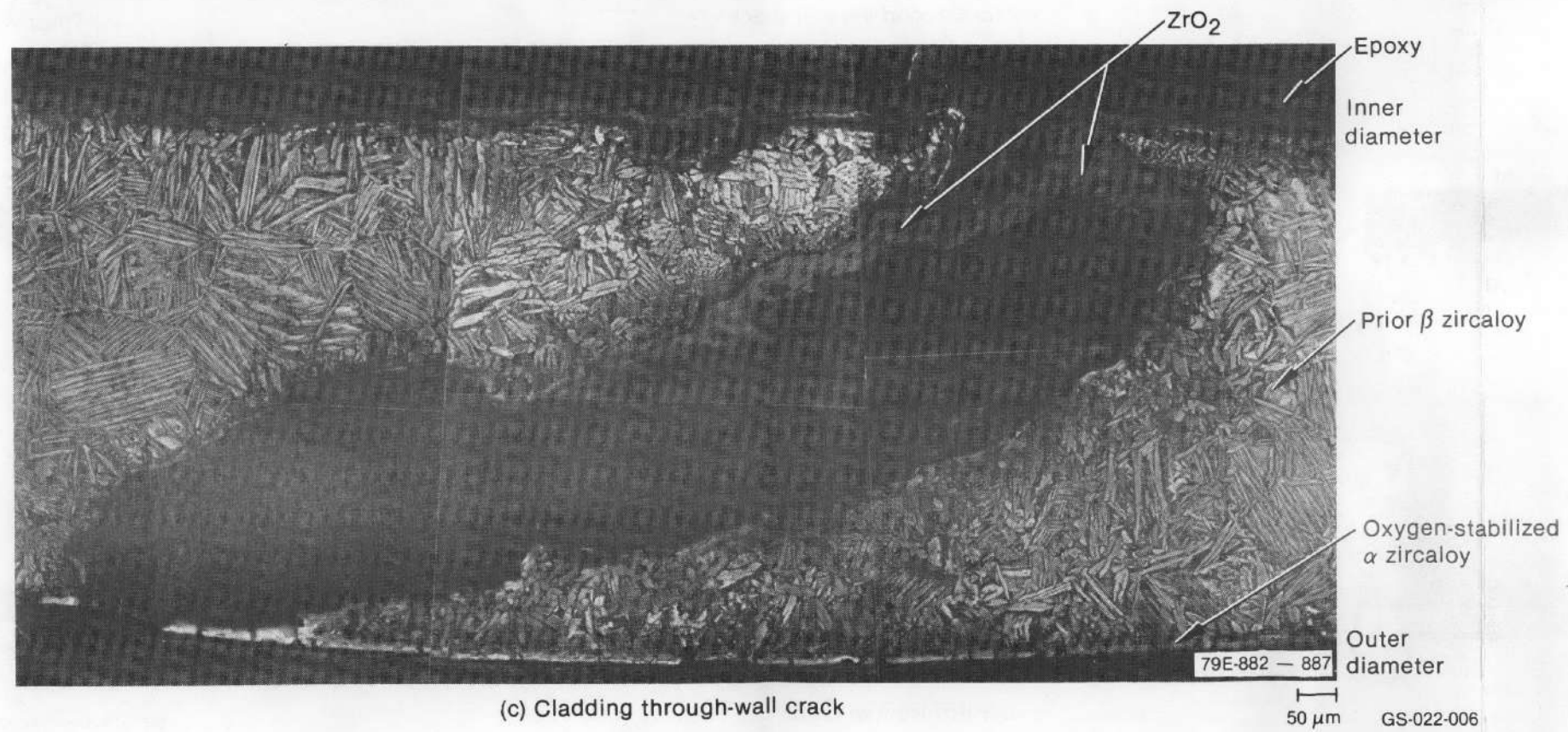
(c) Cladding through-wall crack

Figure 23.   Crack in cladding at the 48-cm elevation of Rod 802-3.

(a) First view of crack

79E-878 — 881

50 μm

(b) Second view of crack

79E-888 — 891

50 μm

(c) Third view of crack

79E-894 — 897

50 μm

(d) Fourth view of crack

79E-914 — 917

50 μm

(e) Fifth view of crack

79E-919, 920

50 μm

(f) Sixth view of crack

79E-921, 922

50 μm

GS-022-003

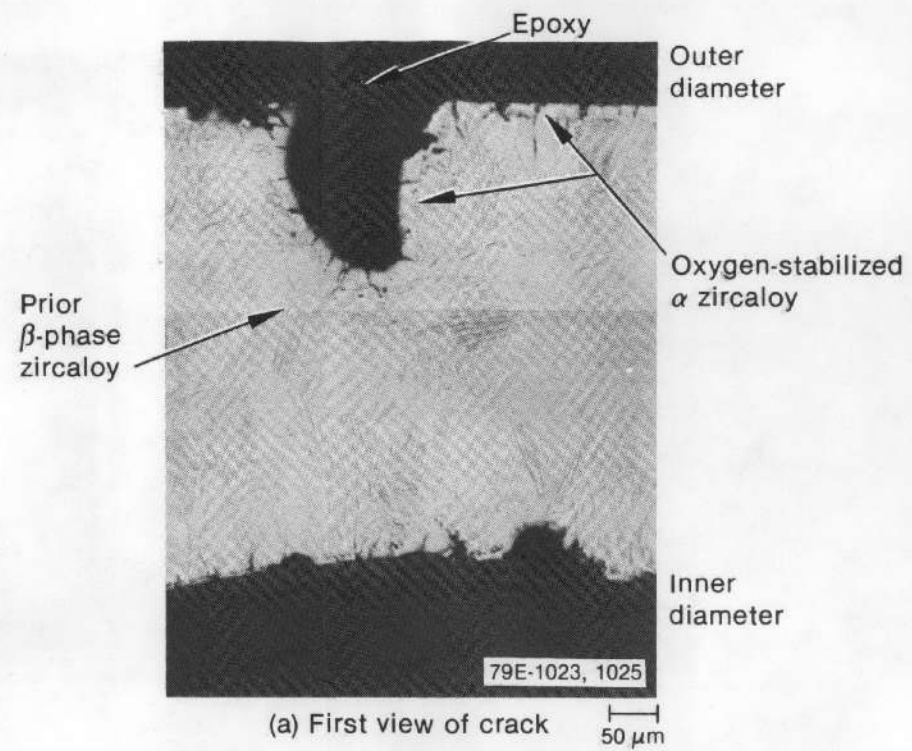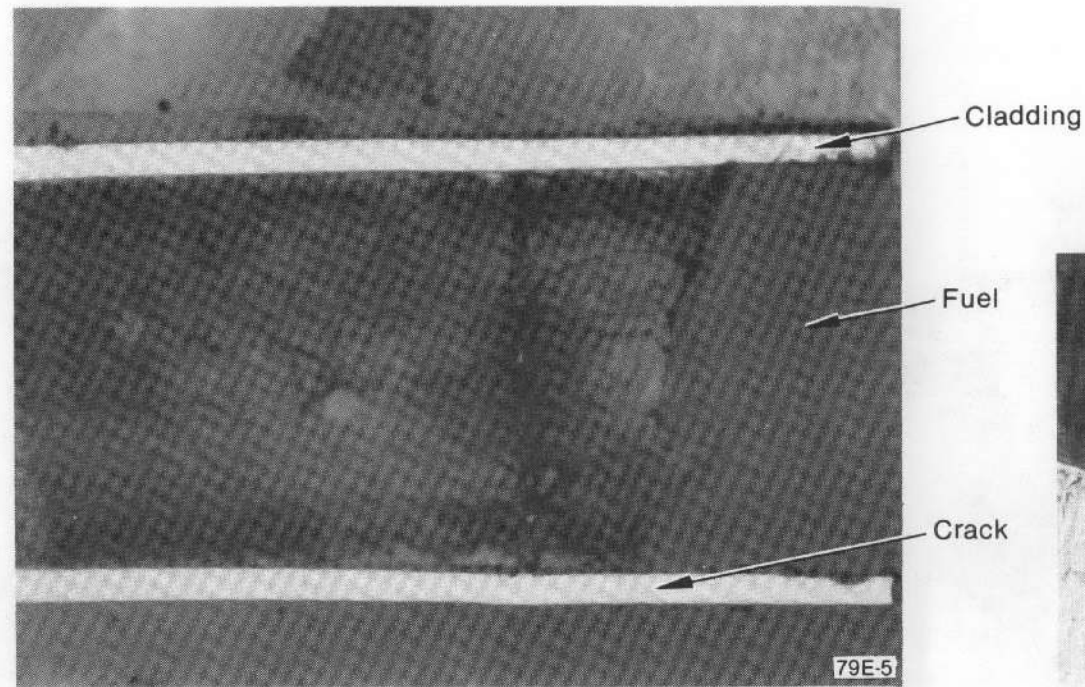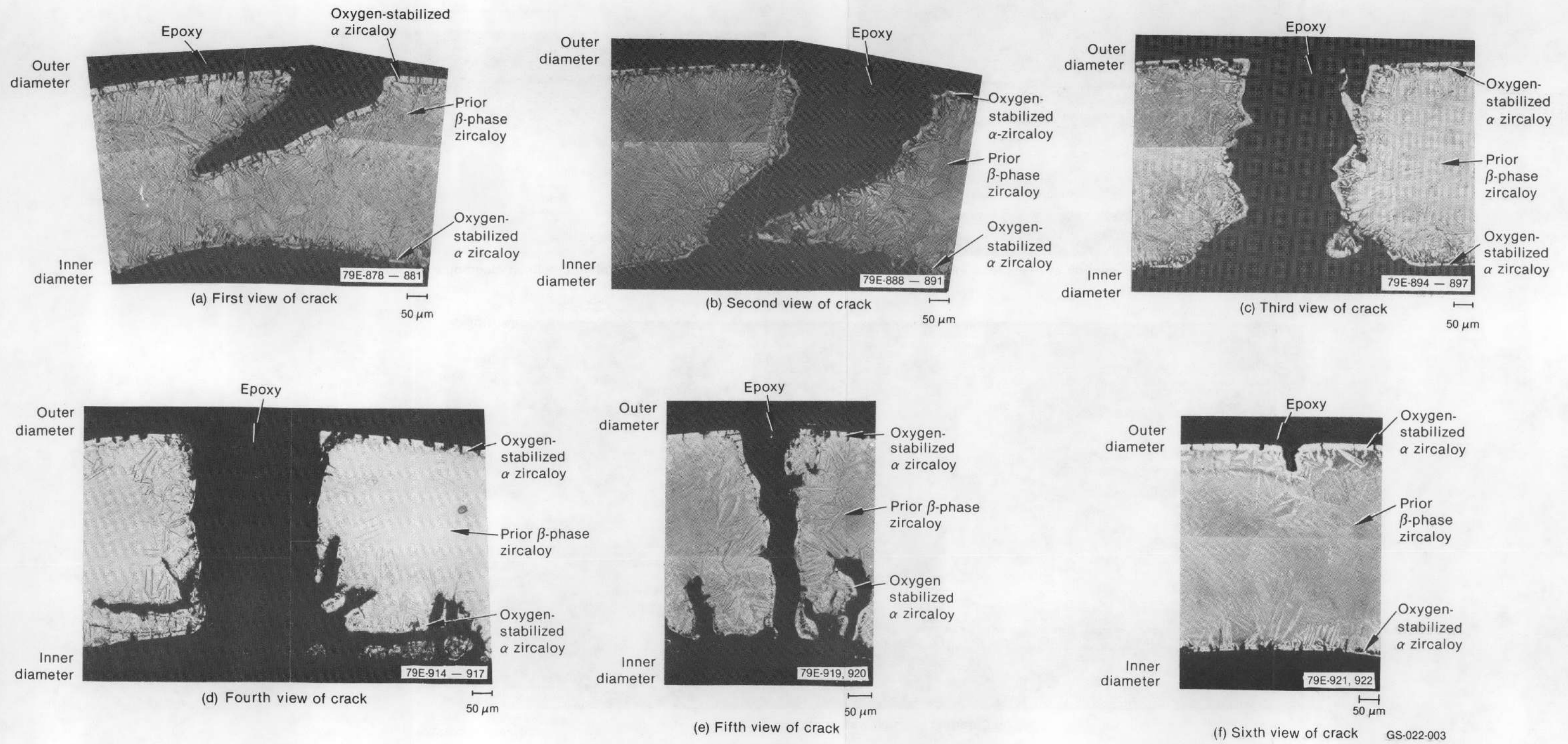Figure 24. Crack in cladding at the 37-cm elevation of Rod 802-3.

30
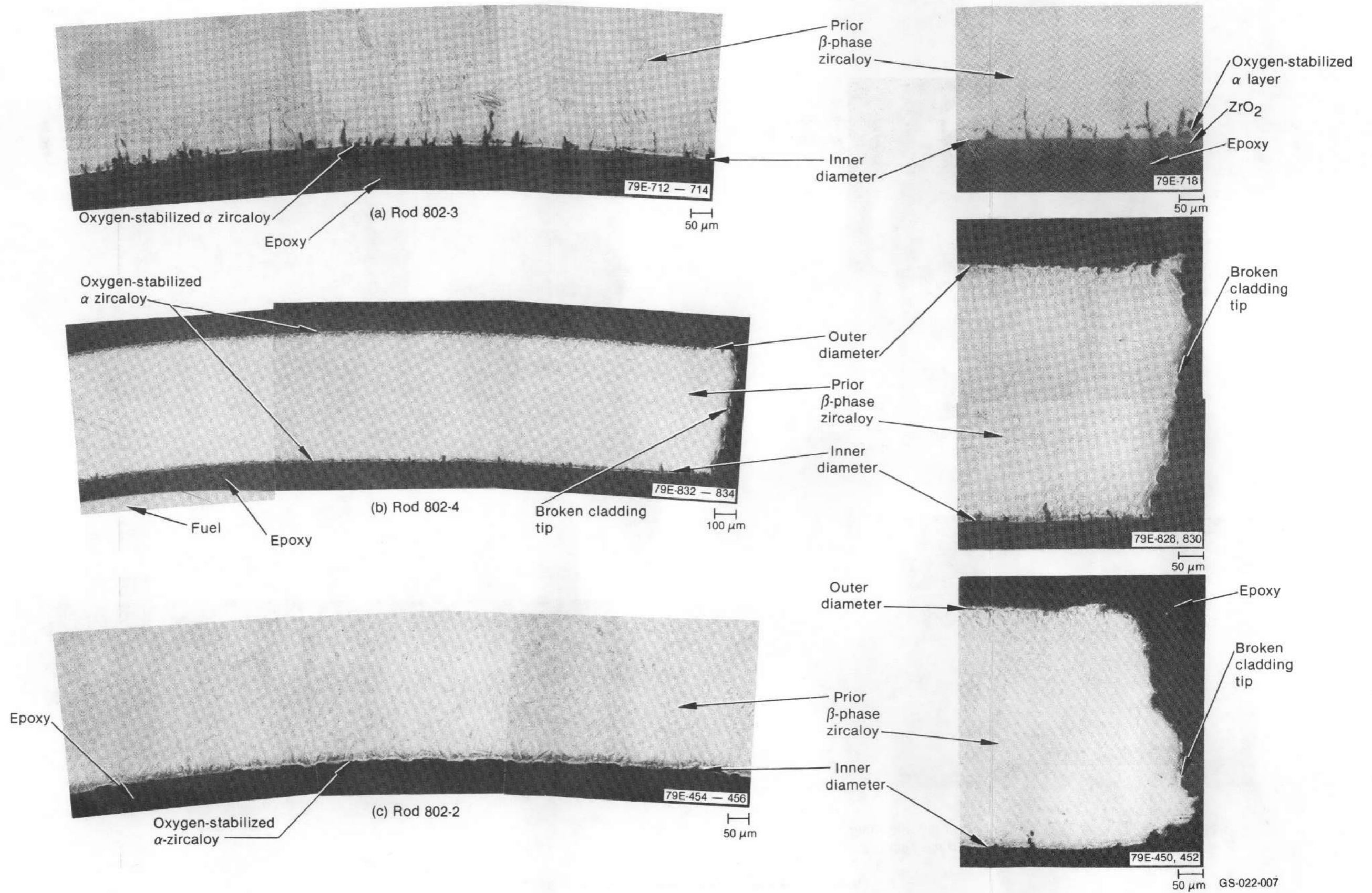
Figure 25. Cracking on the inner surface of the cladding of Rods 802-3, 802-4, and 802-2 when stressed at low temperatures.

31
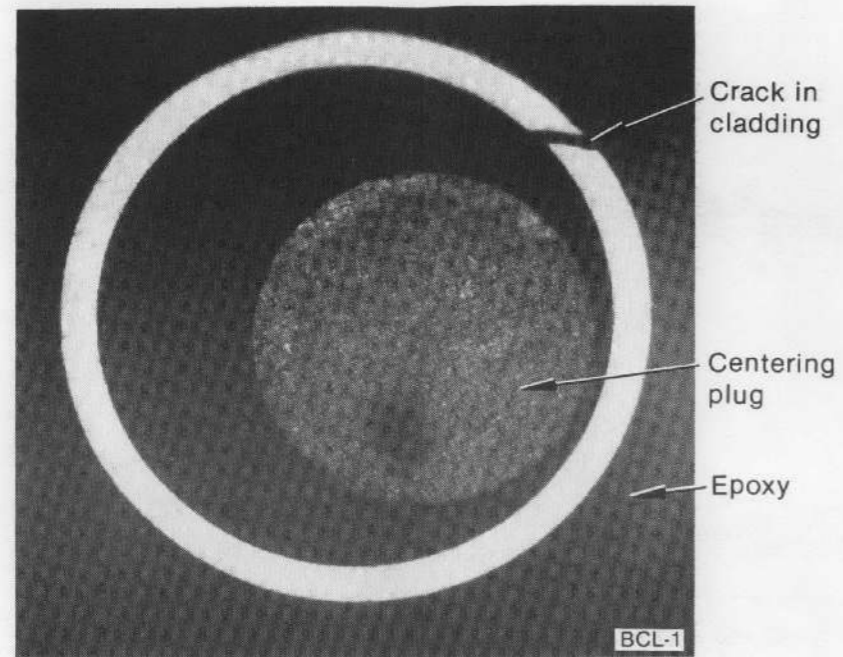
(a) Transverse sample at crack elevation

Crack in cladding

Centering plug

Epoxy

BCL-1

14.3 mm
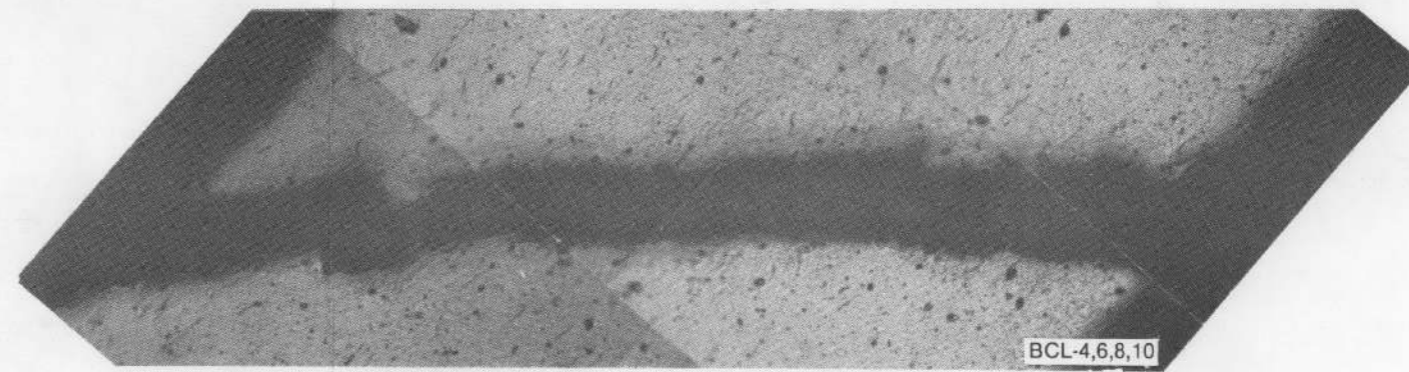
(b) Cladding through-wall crack, bright field

BCL-4,6,8,10
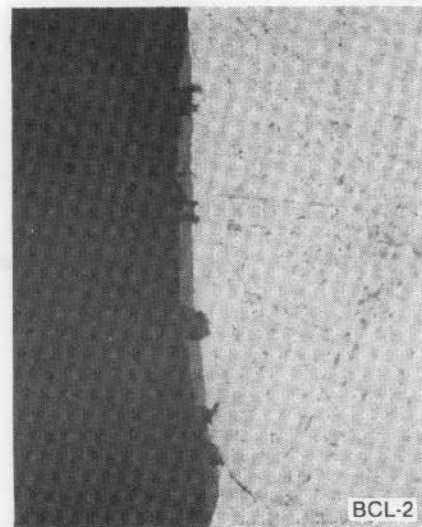
40 μm

(d) Cladding outer surface away from crack

BCL-2

20 μm
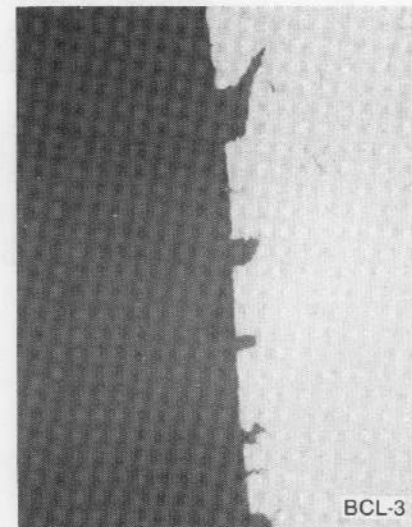
(e) Cladding inner surface near crack

BCL-3

20 μm
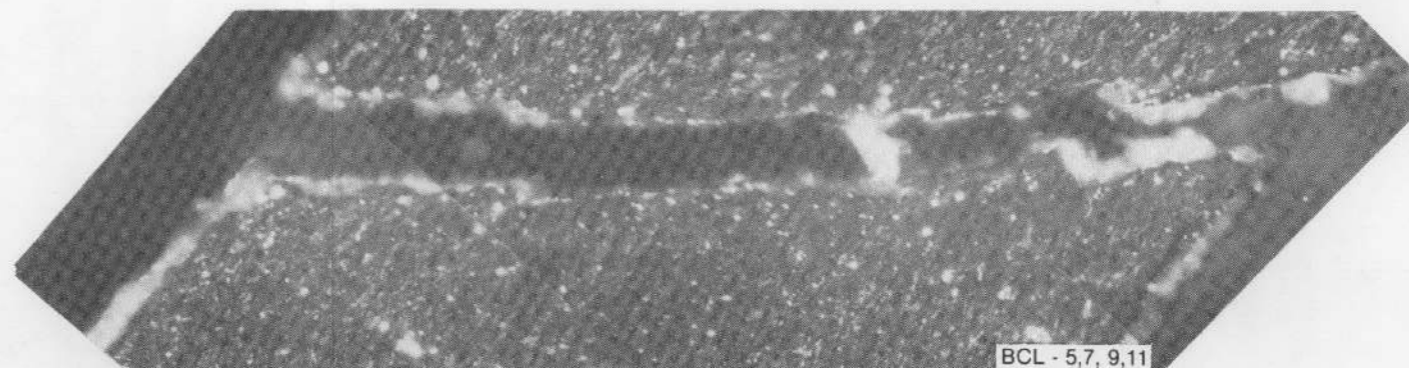
(c) Cladding through-wall crack, polarized light

BCL - 5,7, 9,11

40 μm

GS-022-008

Figure 26. Cracking in expanding mandrel sample from Battelle Columbus Laboratories.

fuel rod was mounted longitudinally and the crack was ground into. The two cracks in Figure 23(b) coincide with the position where the fuel pellets would probably contact the cladding. Again, it is not clear whether the through-wall crack shown in Figure 23(c) initiated on the outside or inside surface. It is highly probable that the cladding continued to deform after the failure occurred, by pellet-cladding mechanical interaction due to differential thermal expansion between the fuel and cladding, thereby opening up the crack.

The crack at 37 cm (Figure 24) was mounted transversely and ground completely through. The view at the highest axial location shows the crack halfway through the cladding wall, beginning on the outside surface and angling sharply toward the inside. The crack progressed through the cladding, becoming very wide (0.415 mm maximum) and straight through the wall. The width of the crack was probably a result of deformation by pellet-cladding mechanical interaction subsequent to the cracking. The crack eventually narrowed, and the lowest elevation view shows a remnant of the crack at the outside surface. The total crack length was 4.3 mm.

No through-wall cracks were found in any of the other three fuel rods. However, during one portion of the posttest examination, some incipient cracks were initiated on the inside surface of the cladding from Rods 802-2 and 802-4. A small half-ring was cut from each of the rods and flattened. All of the samples fractured axially down the middle of the sample. The broken sections were mounted and examined. Figure 25 shows numerous incipient cracks on the inside surface of the cladding from Rod 802-3, which is typical of many of the locations examined on the rod before posttest mechanical deformation. Similar cracking occurred on the inside of the Rod 802-4 cladding and, to a very limited extent, on Rod 802-2 near the fresh fracture surface. The inner surface cracking was not observed at any other locations on Rods 802-2 and 802-4 besides those that were mechanically deformed posttest.

The oxidation of the fracture surfaces made it impossible to determine the fracture mode from the fracture surface appearance. The surfaces of the cracks were masked by the oxidation, making the crack shape somewhat misleading. The cracks may have originally had sharp corners at the cladding inside and outside surfaces before the oxidation.

Expanding mandrel tests have been performed at Battelle Columbus Laboratories[19] on irradiated zircaloy cladding samples. One of the specimens is shown in Figure 26. The major through-wall crack is at the same angle to the radial direction in the cladding as that observed in many of the cracks on Rod 802-3. The edges of the crack are sharper in the out-of-pile expanding mandrel test, but the crack was not oxidized after rod failure. Some incipient cracks were observed on the cladding inside and outside surfaces [Figure 26(d) and (e)] from the purely mechanical stress put on the cladding during the expanding mandrel test. The similarity in appearance between the failures and incipient cracks in the expanding mandrel tests and Rod 802-3 from Test RIA 1-2 indicates that the failure of Rod 802-3 may have been due strictly to mechanical overstressing of the cladding. However, as discussed previously, there is no apparent reason for the stress on the cladding of Rod 802-3 to have been drastically different from that experienced by the other low pressure rod, Rod 802-1.

The pretest rod geometry and the posttest mechanical properties of the zircaloy were examined. The pretest geometry was characterized by overall photographs, neutron radiographs, and profilometry. These data are presented in detail in Appendix B. In general, no major differences were observed in the overall appearance of the rods. The outer diameter of all rods was within 0.84% of the nominal diameter. The neutron radiographs did not show any unusual disturbances in the fuel stack, i.e., gaps in the stack or unusual cracking. The pulsed eddy current (PEC) scans did not indicate any incipient cracks on the inner surface of the cladding of any of the four fuel rods before PBF testing; however, the PEC scans cannot detect defects less than 0.152 mm deep (one-fourth of the cladding nominal wall thickness of 0.622 mm).

The microhardness of the cladding was measured for each rod to provide an indication of changes in mechanical properties that might affect the rod failure threshold. The measured microhardnesses are presented in Table 5 for locations near the outer surface, at the center, and near the inner surface of the cladding wall for several elevations of each rod. Generally, the nominal room temperature hardness of as-received, stress relieved zircaloy has been measured over a range of hardnesses near 260 diamond pyramid hardness (DPH), and, as the cold-work begins to anneal

Table 5. Microhardness of RIA 1-2 test rod cladding

Rod Number	Elevation from Bottom of Fuel Stack (cm)	Microhardness (DPH)		
		Outer Diameter	Center	Inner Diameter
802-1	13.8	295	223	223
		288	223	223
802-1	52.4	357	182	235
		357	174	235
		357	—	—
802-1	75.8	357	182	201
		334	215	191
		—	223	201
802-2	45.4	248	174	440
		248	182	382
		—	—	475
802-2	78.4	201	182	191
		201	191	191
802-3	35.9	475	248	728
		—	248	728
		—	248	607
802-3	45.4	278	191	338
		410	201	338
		278	182	338
802-3	48.4	334	211	728
		514	211	728
		557	201	557
802-3	67.2	278	182	557
		278	191	991
		557	182	514
802-3	Near crack	382	314	410
		334	357 ⎫ Along	514
		314	334 ⎬ crack	334
		—	410 ⎭	382
802-4	45.4	262	201	223
		248	235	223
		262	201	223

close to the recrystallization temperature at 920 K (the transformation from stress relieved to mixed, irregular shaped alpha grains or preequiaxed alpha structure), the nominal hardness decreases to around 230 DPH. Full recrystallization (920 < T < 1105 K) to an equiaxed alpha-phase structure, with no observable grain growth, produces an additional drop in the hardness to about 190 DPH. The hardness values begin to increase again, as the alpha plus beta two-phase structure develops (1105 < T < 1245 K), to values equivalent to or greater than 280 DPH. Upon transformation to the beta phase (zircaloy temperatures T > 1245 K), the nominal room temperature hardness of the matrix increases to the range of 310 to 350 DPH or more, depending on the oxygen content. The highest hardness values measured have been associated with the oxygen-stabilized alpha, with values ranging from 330 to 800 DPH.[20,21] The microhardness measured at the center of the wall of all samples from the Test RIA 1-2 fuel rods did not exceed the microhardness for alpha plus beta structures. The higher microhardnesses measured at the cladding inner surface, outer surface, and along the through-wall cracks in Rod 802-3 were due to the oxygen-stabilized alpha layer that formed on all cladding surfaces exposed to the coolant or in contact with the fuel. In general, for a given microstructure, Rod 802-3 did not exhibit exceptionally high microhardnesses.

Hydrogen analysis was performed on one sample from each of the fuel rods. The specification for the original cladding tubes used for the Test RIA 1-2 rods was 15 ppm hydrogen. After Saxton irradiation, the hydrogen content in the cladding was generally measured at about 40 ppm. The hydrogen content for the four rods is given in Table 6. The three unfailed rods showed hydrogen levels typical of those measured in the Saxton rods before PBF irradiation. The hydrogen content in the failed rod cladding was four times that observed in the unfailed rods. The hydrogen pickup probably resulted from operating the failed fuel rod in film boiling.

The fuel was examined to determine abnormalities that would result in different thermal expansion of the fuel in Rod 802-3 compared to the other three fuel rods, especially Rod 802-1. The fuel structure at several elevations of all four fuel rods was examined. In general, there had been extensive movement of the porosity in the fuel to the UO_2 grain boundaries at the high power elevation of all rods. The fuel grain growth was slighty greater in Rod 802-3 than in the other rods. The grain diameters are listed in Table 7. The larger grain diameter indicates a slightly higher maximum fuel temperature in Rod 802-3 than in the other rods. The small temperature difference and the resulting increase in thermal expansion of the fuel may have affected the overall stress on the cladding of Rod 802-3. However, the cracking in Rod 802-3 occurred over a large axial length of the rod, including regions where the fuel temperatures were lower than at the peak location of the other rods, and the thermal expansion was less. Therefore, relatively small differences in fuel temperature could not be the major reason for the failure of one low pressure rod but not the other. Also, the larger grain size in Rod 802-3 may have been the result of degraded gap conductance in that rod following failure, when the helium-argon fill gas was replaced by steam.

Table 6. Hydrogen content of Test RIA 1-2 fuel rod cladding

Rod Number	Elevation from Bottom of Fuel Stack (cm)	Hydrogen Content (ppm)[a]
802-1	45.0	38, 30
802-2	45.0	45, 37
802-3	45.0	183, 202
802-4	45.0	0, 7

a. Standards were run before each test; 100 ppm standard resulted in 97 ppm, 30 ppm standard resulted in 34 ppm, 100 ppm standard resulted in 84 ppm.

Table 7. Fuel grain diameters of Test RIA 1-2 rods

Rod Number	Elevation from Bottom of Fuel Stack (cm)	Grain Size (μm)			
		Outer Edge	Second to Edge	Third to Edge	Center
802-1	45.4	2.40	5.50	5.31	5.77
	52.4	2.80	2.78	3.35	3.64
	78.4	2.39	2.91	2.75	2.88
802-2	78.4	2.27	2.55	2.62	2.96
	52.4	3.21	3.57	4.23	4.55
	45.4	3.75	4.17	4.65	5.31
802-3	45.4	2.05	3.17	5.26	7.23
	48.0	2.80	2.99	4.35	6.45
	60.4	1.87	2.50	3.30	4.00
	67.2	2.53	2.88	3.85	4.65
802-4	45.4	2.82	3.82	5.22	5.41
	47.7	2.58	3.17	3.97	4.05

EFFECT OF ROD INTERNAL PRESSURE ON ROD DEFORMATION

Investigating the effect of rod internal pressure on the deformation and failure of a fuel rod during an RIA was one of the main objectives of Test RIA 1-2. Significant differences were observed in the total deformation between the two unfailed, high internal pressure rods and the one unfailed, low pressure rod. The measured posttest deformation of the fuel rods is characterized, and the time of deformation and the possible deformation modes are discussed in the following sections.

Measured Posttest Deformation

The cladding deformation of the four fuel rods was characterized by diameter measurements and visual examination, and correlated with cladding peak temperatures. The cladding strain over the length of the rods is plotted in Figures 27 through 30. The maximum diametral strain for the high pressure rods was twice that of the low pressure rods. The two rods with cladding thermocouples (Rods 802-1 and 802-2) showed more strain than the rods without cladding thermocouples, with corresponding pressures. All four fuel rods collapsed near the ends of the rods.

The temperature differences between the four rods were presented in an earlier section. The high pressure rods operated at lower cladding peak temperatures than the low pressure rods. The failed rod with steam present inside operated at the highest cladding temperature. It was found that the higher the maximum diametral strain, the lower the cladding temperature.
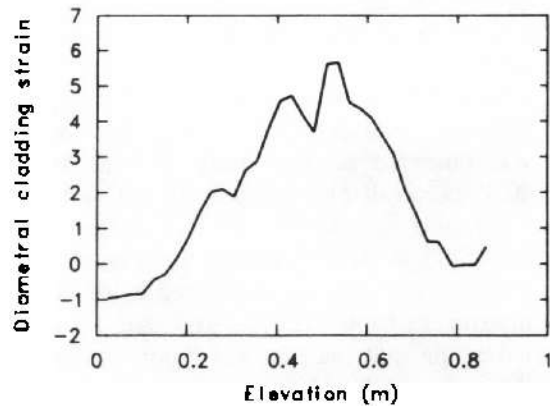

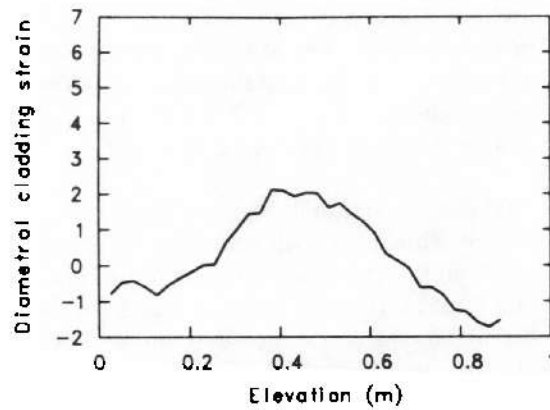Figure 28. Diametral cladding strain of Rod 802-2.
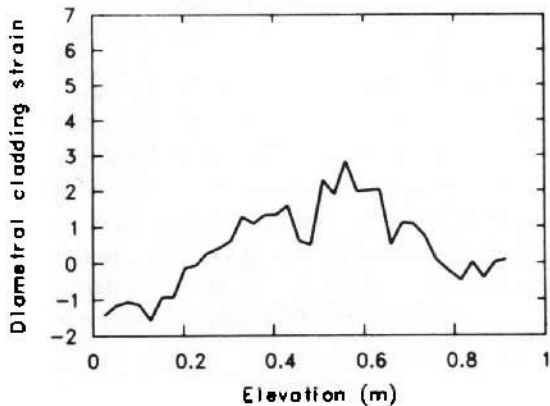

Figure 29. Diametral cladding strain of Rod 802-3.

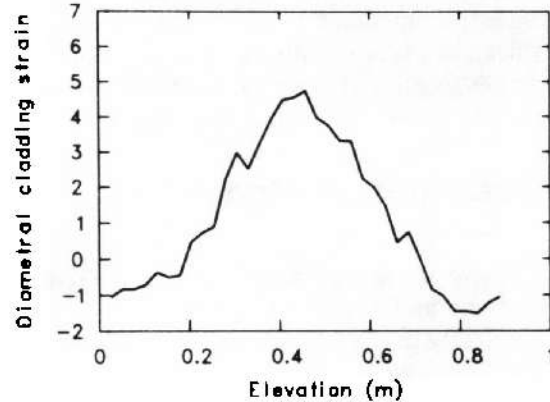

Figure 27. Diametral cladding strain of Rod 802-1.

Figure 30. Diametral cladding strain of Rod 802-4.

37

The observed deformation included ridging of the cladding on the high pressure rods at intervals equal to the length of a fuel pellet, in addition to a maximum of 6% increase in rod diameter. The ridging occurred from 23.5 to 55.4 cm and from 27.1 to 65 cm on high pressure Rods 802-2 and 802-4, respectively. A limited amount of ridging was observed on low pressure Rods 802-1 and 802-3. Overall photographs of rod sections and macrophotographs of rod cross sections showing the ridging are presented in Figures 31, 32, and 33. The ridging correlated with the pellet interfaces of low pressure Rods 802-1 and 802-3, indicating that the fuel was tightly locked within the cladding. No shifting of the fuel stack occurred upon thermal contraction. A crack initiated on the inside surface of the cladding of Rod 802-3 (shown in Figure 22) at the location of maximum deformation. As this crack was polished through, it was found to eventually penetrate the cladding wall. The area of maximum deformation in the high pressure rods did not correlate with fuel pellet interfaces, indicating that the fuel stack was not locked with the cladding upon cooldown. The deformation of Rod 802-2 is shown in Figure 32, and of Rod 802-4 in Figure 33.

The cross section in Figure 32(b) shows that the deformation also included some wall thinning. The wall thickness as a function of orientation for one axial location on Rod 802-2 and the thicknesses for several axial locations on Rod 802-1 are plotted in Figures 34 and 35, respectively. Although the cladding wall thickness of Rod 802-1 averages about 7.5% higher than the nominal thickness of 0.572 mm, the actual wall thickness does not deviate from the average measured thickness at any location by more than 6.3%. Therefore, the initial wall thickness of the cladding of Rod 802-1 was probably 7.5% greater than the nominal pretest thickness. The wall thickness of the cladding of Rod 802-2 at the peak power location (Figure 34) decreased by as much as 27% from the nominal thickness.

Deformation Modes

There are several indications that the rod deformations and the failure of Rod 802-3 occurred very early in the RIA transient. As discussed in a previous section, the oxidation of the inside surface of the through-wall cracks in Rod 802-3 indicated that the crack surfaces were in film boil-

ing as long as the cladding outside surface. The available internal pressure measurement obtained for the high pressure rods during the test was presented in the section titled, "Rod Internal Pressure." Because of the fuel-cladding gap closure, the upper plenum was partially isolated from the heated section of the rod; therefore, no direct information on local pressures and stresses in the deformed region was available. Computer analysis, along with the available information on cladding temperatures, plenum pressures, and posttest examinations, can be used to arrive at a reasonable scenario for the deformation behavior of the rods.

The calculated gap pressure, coolant pressure, permanent hoop strain, and cladding midwall temperature for the high pressure rods for the first 25 s of the test are shown in Figure 36. Nearly all of the deformation was calculated to occur within the first 3 s of the test and is due to the pressure difference between the fuel-cladding gap and the coolant while the cladding is hot. As the gap pressure drops below the coolant pressure at 5 s, the conditions for cladding collapse exist. The cladding does not deform, however, because the cladding temperature has dropped appreciably by that time.

Two cases were modeled for the transient: (a) the internal gas pressure was assumed to be in equilibrium over the entire rod length (FRAP without gas flow model), and (b) the plenum was assumed to be isolated from the heated section of the rod (FRAP with gas flow model). In the first case, the calculated peak strain was only 3% instead of the 6% strain measured. The second case predicted failure of the rod at strains of 400% due to high local gap pressure (~200 MPa) in the high power section of the rod. The measured 6% strain in the high pressure rods indicates a partial isolation of the plenum from the heated section, as opposed to the complete isolation predicted by the FRAP-T5 gas flow model. The low strains calculated without the gas flow model may also be due to the mechanical properties routine in MATPRO, which is based on slow strain rate out-of-pile data.[11] However, the gas flow model is also suspect for an RIA since the model is based on steady state or slow transient data and not for very fast transients.

Ridging of the cladding was observed at axial distances equal to the length of the pellets in all

38

Pellet-to-pellet
interface

Fuel

Cladding

Epoxy

79E-1

Pellet-to-pellet
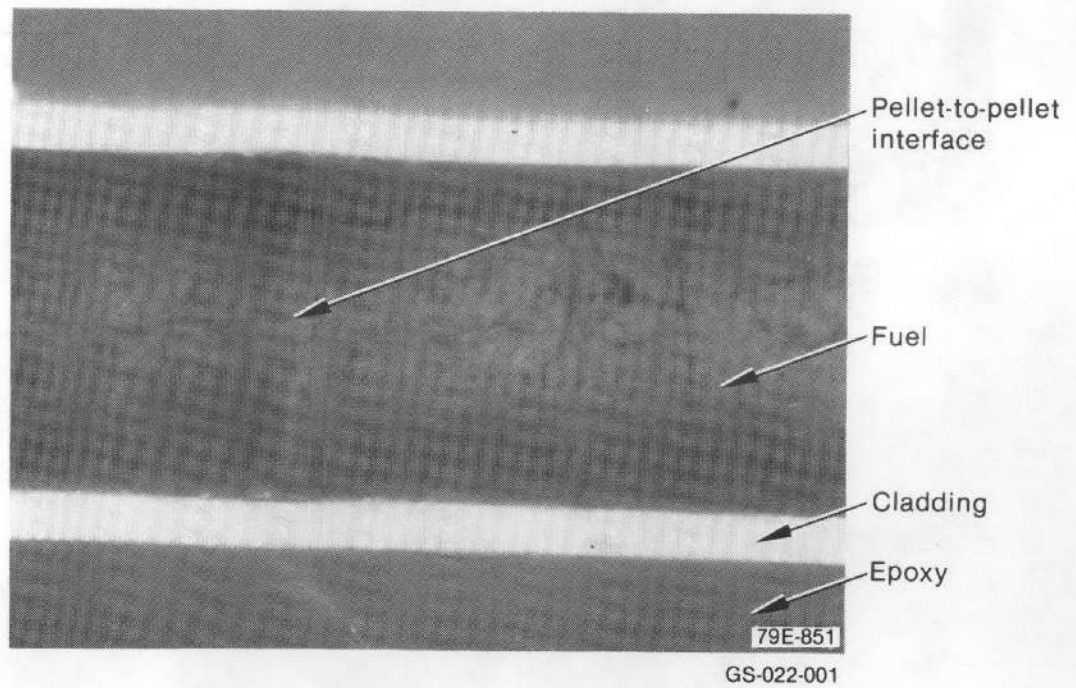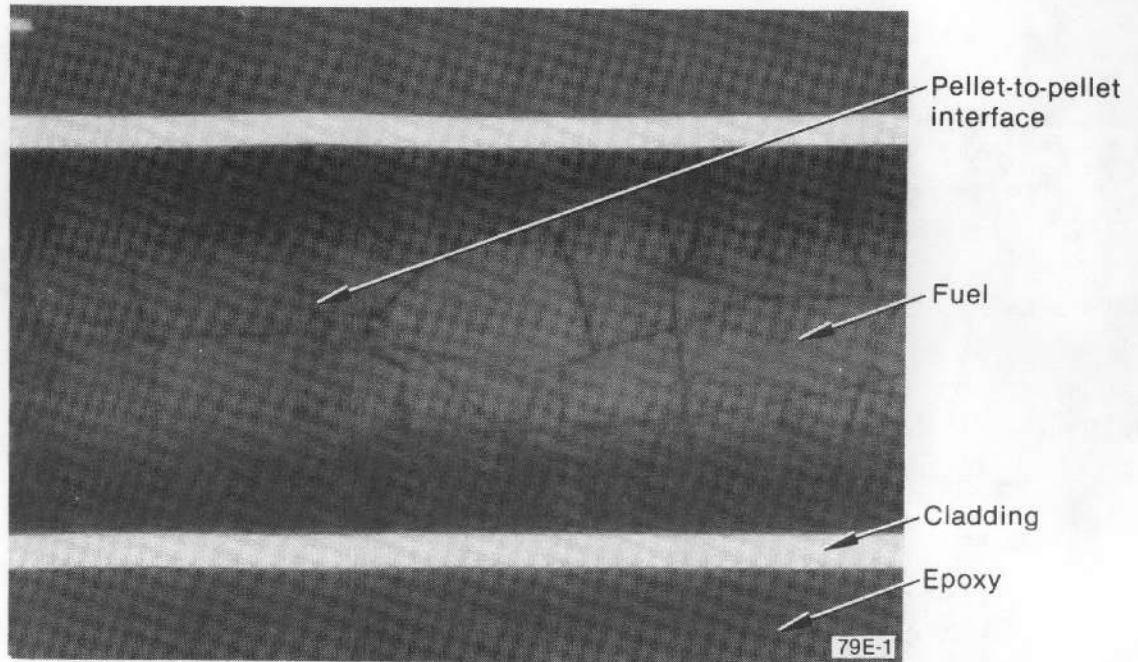interface

Fuel

Cladding
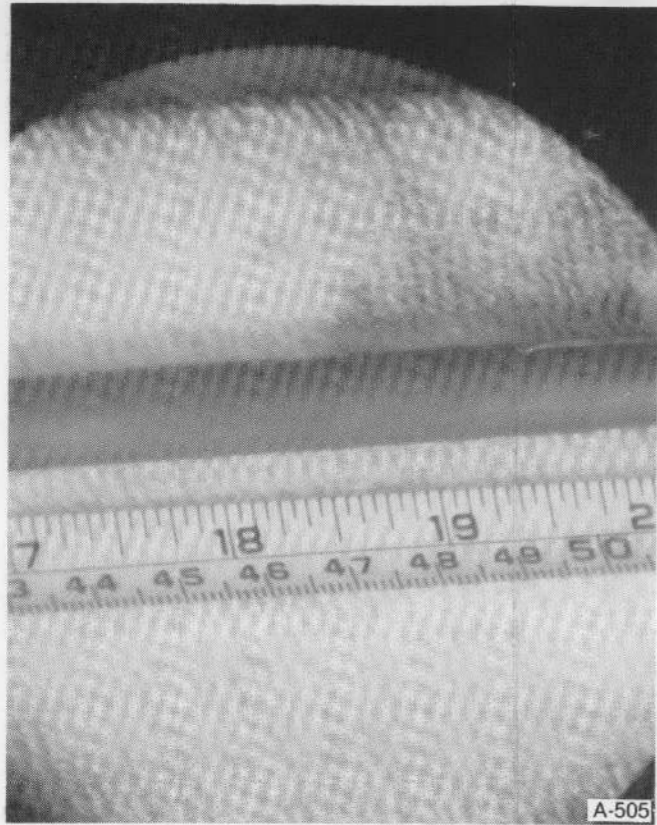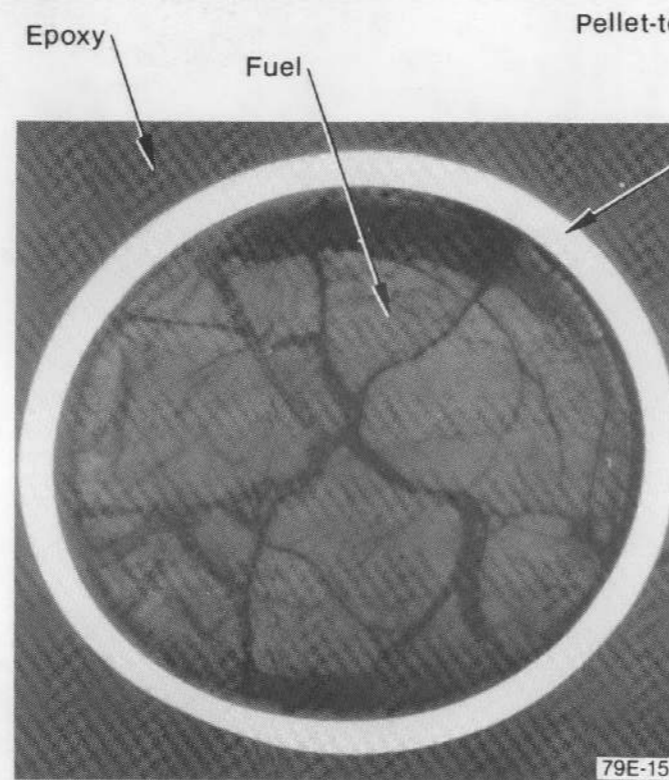
Epoxy

79E-851

GS-022-001

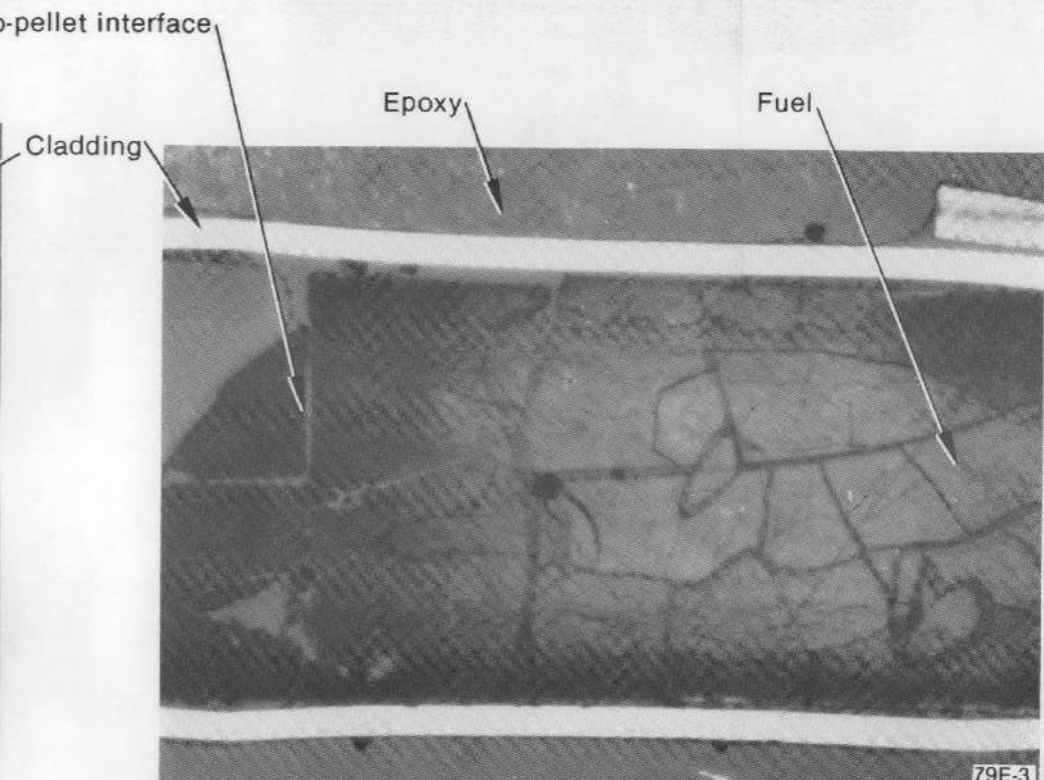Figure 31.   Ridging at pellet interfaces of Rod 802-1.
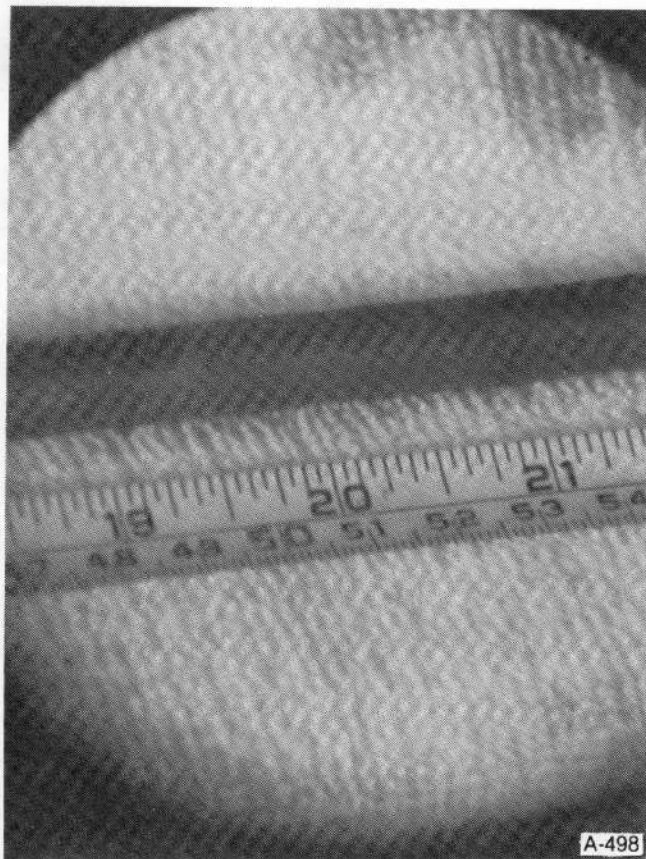
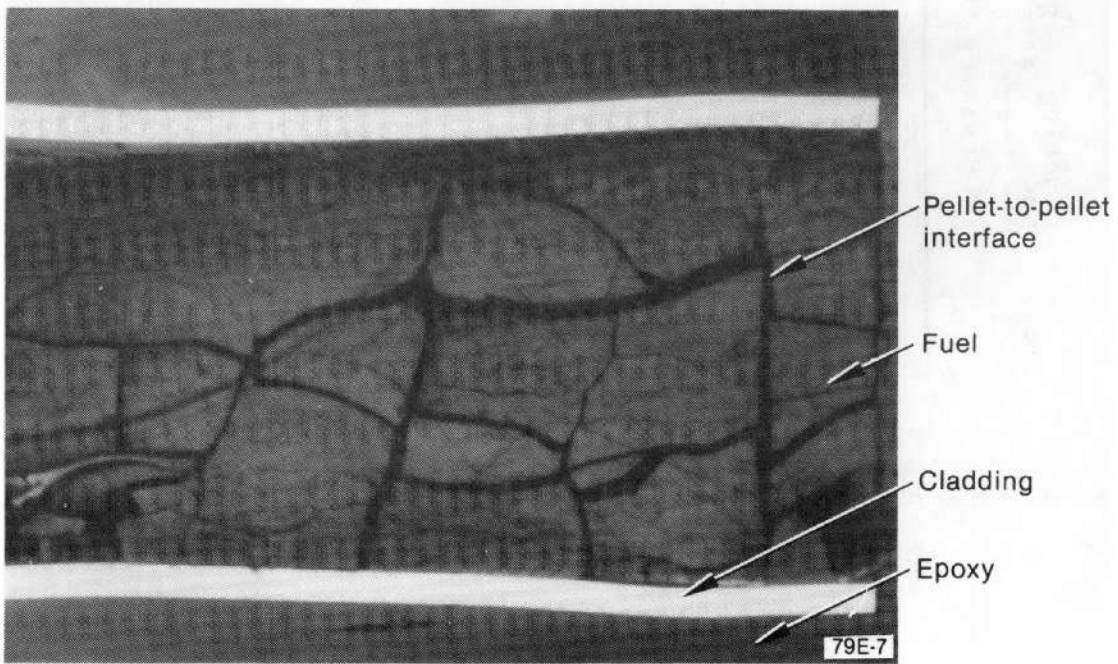(a) Overall view of rod

(b) Transverse sample

(c) Longitudinal sample

GS-022-009

Figure 32.   Deformation of Rod 802-2 cladding.

(a) Overall view of rod

(b) Longitudinal sample

GS-022-002

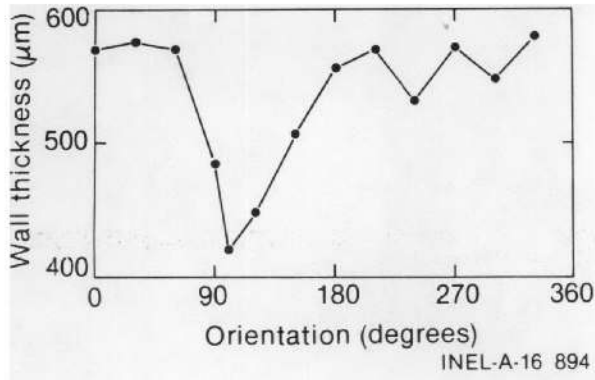Figure 33. Deformation of Rod 802-4 cladding.

41

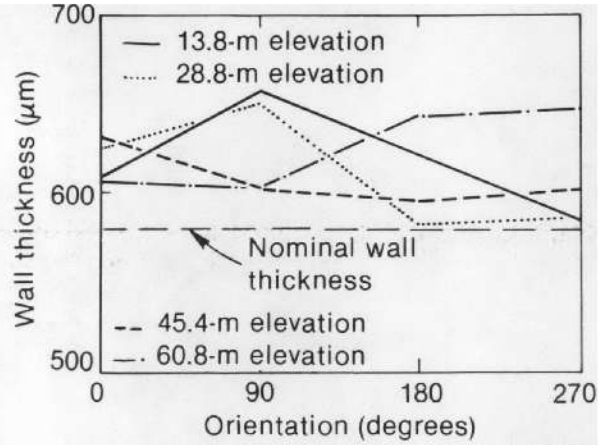Figure 34.   Rod 802-2 wall thickness at 47 cm.

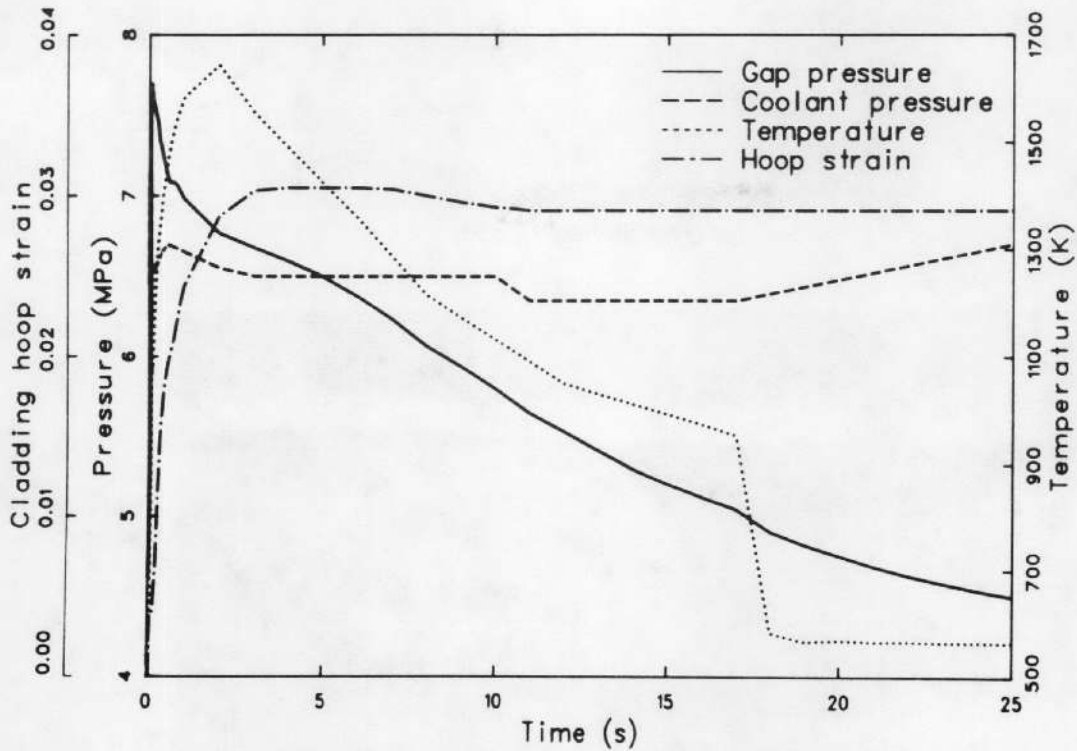Figure 35.   Rod 802-1 wall thickness at four elevations.

Figure 36.   Calculated gap pressure, coolant pressure, permanent hoop strain, and cladding temperature of Rod 802-2.

42

rods. The ridging of the high pressure rods was exaggerated and broadened by overall deformation during the time when the rod internal pressure was higher than the coolant pressure and the cladding was hot. Cladding ridging is usually associated with deformation of the fuel pellets to an hourglass shape because of a parabolic temperature profile through the pellet. Subsequent hard contact of the fuel and cladding results in deformation of the cladding only at the location of the pellet interfaces.

The fuel pellets did not have a parabolic temperature profile during the time that the ridging occurred during Test RIA 1-2, although a very steep temperature gradient did exist near the fuel pellet surface. Within the first 3 s, the fuel pellets had a fairly flat profile through the pellet center, with the fuel peak temperature just inside the pellet surface. The type of pellet deformation that would occur due to this temperature profile is not clear. Apparently, the ends of the fuel pellets are still the first locations to contact the cladding.

CONCLUSIONS

Test RIA 1-2 was a four-rod test operated to obtain peak fuel enthalpy near the failure threshold as determined from the previous SPERT tests with preirradiated fuel rods. This report presented a discussion and analysis of the operation and consequences of Test RIA 1-2.

Conclusions determined on the basis of results from the posttest examination of the fuel rods, on-line data, and computer code calculations are that

1. One of the four fuel rods operated at an axial peak, radial average fuel enthalpy of 185 cal/g failed. This result is consistent with the previously determined failure threshold, in as much as the results from all four rods fall within the statistical uncertainity of the limit.

2. A scenario was determined for the behavior of a fuel rod subjected to an axial peak, radial average fuel enthalpy of 185 cal/g during a hypothetical reactivity initiated accident. Rapid fuel heatup is followed by gap closure, local deformation of the fuel pellet occurs due to the temperature gradient through the pellet, and the cladding deforms (ridging) at the pellet interfaces as a result of fuel deformation. One rod fails at this time. The cladding begins to heat up. In the high pressure rods, the internal pressure exceeds the coolant pressure and the cladding deforms (as much as

6% diametral strain). The low pressure rods deform to a lesser extent (1 to 2%) as a result of the continued thermal expansion of the fuel, followed by stress relief of the hot cladding. Collapse occurs at the ends of the high pressure rods where the internal gas is partially isolated from the rest of the rod due to gap closure, and the internal pressure never exceeds system pressure. The fuel temperature and subsequent thermal expansion of the fuel is less at the ends of the high pressure rods than in the middle, allowing collapse to occur. Collapse is observed at the ends of the low pressure rods also. The cladding continues to oxidize for several seconds after the deformation occurs.

3. The failure mode of Rod 802-3 was not conclusively identified. However, the cracking that occurred is similar to that observed due to pellet-cladding mechanical interaction.

4. The present gas flow model in FRAP over-predicts the isolation of the hot region of the rod from the plenum as a result of gap closure. The axial temperature profile of the rods was flatter than predicted, probably due to incorrect evaluation by the RELAP4 code of the thermal-hydraulic conditions during the RIA transient.

44

REFERENCES

1. *Code of Federal Regulations*, Title 10, Part 50, Appendix A, Criteria 28, "Reactivity Limits," 1979.

2. "Assumptions Used for Evaluating a Control Rod Ejection Accident for Presssurized Water Reactors," *NRC Regulatory Guide 1.77*, May 1974.

3. D. H. Risher, Jr., *An Evaluation of the Rod Ejection Accident in Westinghouse Pressurized Water Reactors Using Spatial Kinetics Methods*, WCAP-7588, December 1971, and Rev. 1-A, January 1975.

4. C. J. Paone et al., *Rod Drop Accident Analysis for Large Boiling Water Reactors*, NED-10527, March 1972.

5. T. Fujishiro et al., *Light Water Reactor Fuel Response During Reactivity Initiated Accident Experiments*, NUREG/CR-0269, TREE-1237, August 1978.

6. Nuclear Regulatory Commission, Division of Reactor Safety Research, *Water Reactor Safety Research Program—A Description of Current and Planned Research*, NUREG-0006, February 1979.

7. T. E. Murley et al., "Summary of LWR Safety Research in the USA," *International Conference on Nuclear Power and Its Fuel Cycle, Salzburg, Austria*, NUREG-0234, May 1977.

8. C. L. Zimmermann et al., *Experiment Data Report for Test RIA 1-2 (Reactivity Initiated Accident Test Series)*, NUREG/CR-0765, TREE-1271, June 1979.

9. K. R. Katsma et al., *RELAP4/MOD5—A Computer Program for the Transient Thermal-Hydraulic Analysis of Nuclear Reactors and Related Systems, User's Manual, Volume I, RELAP4/MOD5 Description*, ANCR-NUREG-1335, September 1976.

10. L. J. Siefken et al., *FRAP-T5—A Computer Code for the Transient Analysis of Oxide Fuel Rods*, NUREG/CR-0840, TREE-1281, June 1979.

11. D. L. Hagrman, G. A. Reymann, R. E. Mason (eds.), *MATPRO—Version 11 (Revision 1)—A Handbook of Materials Properties for use in the Analysis of Light Water Reactor Fuel Rod Behavior*, NUREG/CR-0497, TREE-1280, Revision 1, February 1980.

12. J. B. Cathcart et al., *Zirconium Metal-Water Oxidation Kinetics IV, Reaction Rate Studies*, ORNL/NUREG-17, August 1977.

13. A. F. Brown and T. Healey, "The Kinetics of Total Oxygen Uptake in Steam-Oxidized Zircaloy-2 in the Range 1273-1673 K," *Journal of Nuclear Materials, 88*, 1980, pp. 1-6.

14. R. S. Semken et al., *Reactivity Initiated Accident Test Series, RIA Scoping Tests Fuel Behavior Report*, NUREG/CR-1360, EGG-2028, April 1980.

15. S. L. Seiffert et al., *Reactivity Initiated Accident Test Series, Test RIA 1-1 Fuel Behavior Report*, NUREG/CR-1465, EGG-2040, September 1980.

16. R. W. Miller, *The Effects of Burnup on Fuel Failure*, ANCR-1280, January 1976.

17. G. W. Gibson et al., *Characteristics of UO_2-Zircaloy Fuel Rod Materials From the Saxton Reactor for Use in Power Burst Facility*, ANCR-NUREG-1321, September 1976.

18. J. T. A. Roberts et al., "On the Pellet-Cladding Interaction Phenomenon," *Nuclear Technology, 35,* Mid-August 1977, pp. 131-144.

19. *Battelle-Columbus Laboratory Quarterly Progress Report,* January-March 1978.

20. S. L. Seiffert and R. R. Hobbins, *Oxidation and Embrittlement of Zircaloy-4 Cladding from High Temperature Film Boiling Operation,* NUREG/CR-0517, TREE-1327, April 1979.

21. R. R. Hobbins et al., "Zircaloy Cladding Behavior During Irradiation Tests Under Power-Cooling-Mismatch Conditions," *American Society for Testing and Materials,* ASTM STP 633, 1977, pp. 182-208.

EG&G Idaho, Inc.
P.O. Box 1625
Idaho Falls, Idaho 83415